Thalamus and claustrum control parallel layer 1 circuits in retrosplenial cortex

Ellen K.W. Brennan[1,2*], Izabela Jedrasiak-Cape[1*], Sameer Kailasa[3], Sharena P. Rice[1,2], Shyam Kumar Sudhakar[1], & Omar J. Ahmed[1,2,4,5,6,#]

[1]Dept. of Psychology,
[2]Neuroscience Graduate Program,
[3]Dept. of Mathematics,
[4]Michigan Center for Integrative Research in Critical Care,
[5]Kresge Hearing Research Institute,
[6]Dept. of Biomedical Engineering,
University of Michigan, Ann Arbor, MI 48109.

*Co-first authors
[#]Lead Contact & Corresponding Author

Lead Contact & Corresponding Author:
Omar J. Ahmed
Mail: Dept. of Psychology, 530 Church St. University of Michigan, Ann Arbor, MI 48109
Email: ojahmed@umich.edu
Phone: 734-764-3853

ABSTRACT

The granular retrosplenial cortex (RSG) is critical for both spatial navigation and fear conditioning, but the neural codes enabling these seemingly disparate functions remain unknown. Here, using optogenetic circuit mapping, we reveal a double dissociation that allows parallel circuits in superficial RSG to process navigation- versus fear-related inputs. The anterior thalamus, a source of head direction information, strongly recruits small, low rheobase (LR) pyramidal cells in RSG layer 3. Neighboring regular-spiking (RS) cells are instead preferentially controlled by claustral and anterior cingulate inputs, sources of higher-order and fear-related information. Precise sublaminar axonal and dendritic arborization within RSG layer 1 enable this parallel processing. Synaptic dynamics and computational modeling suggest LR neurons are optimally-tuned conjunctive encoders of direction and distance inputs from the thalamus and dorsal subiculum, respectively. RS cells are better positioned to support contextual fear memories. Thus, parallel input streams to computationally-distinct principal neurons help facilitate diverse RSG functions.

INTRODUCTION

The retrosplenial cortex (RSC) is a densely connected cortical region essential for spatial learning, memory, and navigation (Alexander et al., 2020; Alexander and Nitz, 2017; Chrastil, 2018; Hinman et al., 2018; Spiers and Barry, 2015; Todd and Bucci, 2015; Valenstein et al., 1987; Vann et al., 2009), as well as contextual fear conditioning (Corcoran et al., 2011; Keene and Bucci, 2008a, 2008b; Kwapis et al., 2015; Yamawaki et al., 2019b, 2019a). The superficial layers of the granular RSC (RSG) contain two subtypes of principal excitatory pyramidal neurons that have strikingly distinct physiology, morphology, and computational capabilities: the low-rheobase (LR) neuron and the regular-spiking (RS) neuron (Brennan et al., 2020; Kurotani et al., 2013; Yousuf et al., 2020). The RSG receives inputs from many regions, including the anterior thalamus (Ichinohe et al., 2008; O'Mara, 2013; Shibata, 1993; van Groen and Wyss, 1995; Yamawaki et al., 2019b), subiculum (Yamawaki et al., 2019a, 2019b, Opalka et al., 2020; Nitzan et al., 2020), hippocampus (Alexander et al., 2018; Wyss and van Groen, 1992; Yamawaki et al., 2019b), claustrum (van Groen and Wyss, 2003, 1990; Wang et al., 2017), and cingulate cortex (van Groen and Wyss, 1990, 2003), among others. However, the precise nature of many of these inputs and their relative connectivity with these two distinct superficial subtypes has not yet been documented. Such knowledge is critical to develop a mechanistic understanding of how the RSG integrates information from multiple sources to carry out the computations necessary to support its unique spatial- and fear-related memory functions.

In order to facilitate a wide variety of functions, cortical regions, including the RSG, integrate projections from one or more thalamic nuclei (Herkenham, 1986, 1980; Jones, 2001, 1998; Peters, 1979; van Groen and Wyss, 1995). Thalamocortical (TC) relay cells (Clascá et al., 2012) are often grouped into three distinct types of nuclei: core nuclei targeting layer 4 of specific sensory cortices, intralaminar nuclei predominantly targeting deep cortical layers, and paralaminar/ventral midline (matrix) nuclei projecting predominantly to layer 1 of widespread cortical regions (Hanbery and Jasper, 1953; Herkenham, 1986; Jones, 2001, 1998; Morison and Dempsey, 1941; Rubio-Garrido et al., 2009). Matrix cells outnumber core cells but are comparatively understudied (Rubio-Garrido et al., 2009). Contrary to their original classification by Lorento de No as "nonspecific" (Lorento de No, 1938), distinct matrix nuclei project to specific cortical regions with sublaminar specificity (Anastasiades et al., 2020; Cruikshank et al., 2012; Yamawaki et al., 2019b). These projections result in subtype-specific activation of cortical inhibitory neuronal subtypes, both in layer 1 (Anastasiades et al., 2020; Cruikshank et al., 2012) and in deeper layers (Delevich et al., 2015), to provide temporally precise regulation of cortical activity (Cruikshank et al., 2012). These inputs also target excitatory neurons (Collins et al., 2018; Cruikshank et al., 2012; Guo et al., 2018; Rodriguez-Moreno et al., 2020; Rubio-Garrido et al., 2009; Van Der Werf et al., 2002; Yamawaki et al., 2019b). While layer 5 pyramidal subtypes in visual cortex have been anatomically shown to receive differential proportions of synapses from various

thalamic nuclei (Kim et al., 2015), it is not known whether there are subtype-specific physiological differences in terms of the functional matrix inputs onto neighboring cortical pyramidal cells, particularly in the RSG.

The cortex, including the RSG, also receives widespread inputs from the densely connected claustrum (Brown et al., 2017; Crick and Koch, 2005; Goll et al., 2015; Jackson et al., 2018; Kim et al., 2016; Narikiyo et al., 2020; Wang et al., 2017; White and Mathur, 2018). As with TC signaling, the claustrum innervates both excitatory (Da Costa et al., 2010; Narikiyo et al., 2020) and inhibitory (Jackson et al., 2018; Narikiyo et al., 2020; Salerno et al., 1984) neurons via precise laminar targeting (Wang et al., 2017) and projects to many of the same cortical regions as the thalamus (Burman et al., 2011). Claustrocortical (ClaC) projections are thought to regulate complex cortical functions (Crick and Koch, 2005; Goll et al., 2015; Jackson et al., 2018; Kitanishi and Matsuo, 2017; Narikiyo et al., 2020; Renouard et al., 2015; Smith et al., 2012; White and Mathur, 2018), including the coordination and amplification of correlated signals across cortical regions, thus facilitating integration of temporally relevant information (Kim et al., 2016; Smith et al., 2012; Smythies et al., 2012). The claustrum is also implicated in fear conditioning, with increased claustral activity reported in human phobias (Ipser et al., 2013) and shock and fear conditioning in animal studies (Cho et al., 2017; Vakolyuk et al., 1980). While TC and ClaC signaling both serve as critical regulators of cortical processing, it is not known if they do so via parallel or integrative control of target excitatory neurons. Here, we use channelrhodopsin (ChR2)-assisted circuit mapping to study the subtype-specific synaptic effects of anterior thalamic versus claustral input to the RSG. Our results reveal a double dissociation that can allow navigation- versus fear-related inputs to be processed by computationally distinct LR and RS neurons in the superficial RSG.

RESULTS

Cell-type specific thalamic control of pyramidal cells in layer 3 of RSG

Layer 3 of the granular retrosplenial cortex (RSG) contains two principal pyramidal neurons: the low-rheobase (LR) neuron and the regular-spiking (RS) neuron (Brennan et al., 2020; Kurotani et al., 2013; Yousuf et al., 2020). Using whole-cell patch clamp recordings, we again identified LR and RS neurons by their unique intrinsic properties, predominantly the low rheobase, high input resistance, lack of adaptation, and narrow spike width of LR neurons compared to RS neurons (Figure 1A-C, Figure S1, & Table 1; Brennan et al., 2020). We used channelrhodopsin-assisted circuit mapping (CRACM) to interrogate inputs to these two cell types. Consistent with previous studies (Odagiri et al., 2011; van Groen and Wyss, 2003, 1990; Yamawaki et al., 2019b), virus injections into the anterodorsal and anteroventral thalamic nuclei (AD/AV) resulted in ChR2-eYFP being expressed in thalamocortical (TC) axons and terminals in layer 1a (L1a; the most superficial part of layer 1) and in layer 3 (L3) of superficial RSG (Figure 1D&E). To test whether these thalamocortical inputs target the LR and RS neurons in layer 3, we stimulated the thalamic axons and terminals with 1 ms pulses at a 10 Hz frequency for 1 second at maximum LED power over the cell body of the patched neurons (Figure 1F; see Methods). From resting membrane potentials of approximately -65 mV, LR neurons were strongly driven past spike threshold by these thalamic inputs while RS neurons exhibited far smaller EPSPs, typically not exceeding 1 mV even at this maximal light intensity (Figure 1G). To quantify the impact of TC inputs on LR and RS spike rates, we next depolarized the cells until they were spiking at 10-25 Hz and delivered a single LED pulse (see Methods). To rule out effects of feed-forward inhibition in these experiments, the $GABA_A$ antagonist, picrotoxin (50 µM), was added to the bath. Compared to their baseline rates, such stimulation evoked a significant increase in spiking in LR neurons ($p = 0.002$, Wilcoxon rank sum test) but not RS neurons ($p = 0.19$, Wilcoxon rank sum test; Figure 1H). The LR neurons thus had a significantly larger increase in spike count evoked by the optical pulse than RS neurons ($p = 0.0012$, Wilcoxon rank sum test; Figure 1I). This suggested that LR neurons receive stronger activation from TC inputs than their neighboring L3 RS neurons.

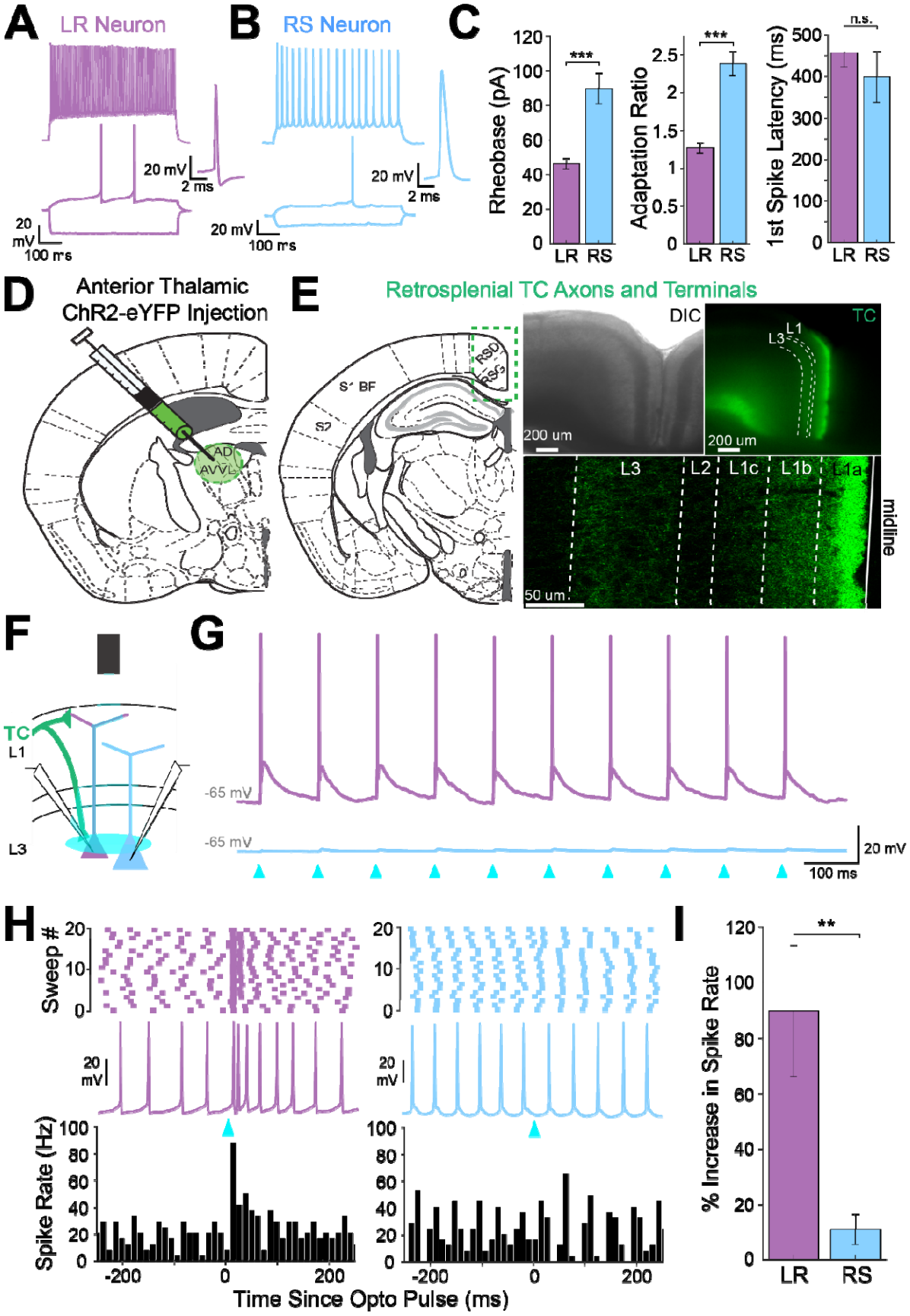
A
LR Neuron
20 mV
2 ms
20 mV
100 ms
B
RS Neuron
20 mV
2 ms
20 mV
100 ms
C
Rheobase (pA)
***
LR RS
Adaptation Ratio
***
LR RS
1st Spike Latency (ms)
n.s.
LR RS
D
Anterior Thalamic
ChR2-eYFP Injection
AD
AVVL
E
Retrosplenial TC Axons and Terminals
S1 BF
S2
RSD
RSG
DIC
200 um
TC
L1
L3
200 um
L3
L2
L1c
L1b
L1a
midline
50 um
F
TC
L1
L3
G
-65 mV
-65 mV
20 mV
100 ms
H
Sweep #
20 mV
Spike Rate (Hz)
-200
0
200
Time Since Opto Pulse (ms)
I
% Increase in Spike Rate
**
LR
RS

Figure 1. Anterior thalamic input controls LR, but nor RS, neurons in superficial granular retrosplenial cortex.

A. Representative example of the firing properties of LR neurons. Top trace: sustained high-frequency firing of action potentials with little spike frequency adaptation at high current inputs. Bottom trace: Delay to first spike at threshold current inputs and little sag with hyperpolarization. Right inset is a zoomed in view of the first spike from near-threshold current input.

B. Same as ***A,*** but for a representative RS neuron. Note the spike frequency adaptation at high current inputs, delay to first spike at near-threshold current inputs, and pronounced sag with hyperpolarization.

C. Bar graphs showing population data comparisons between LR and RS neurons of the following intrinsic properties: rheobase ($p<0.001$; Wilcoxon rank sum), adaptation ratio ($p<0.001$; Wilcoxon rank sum), and latency to first spike ($p=0.3271$; Wilcoxon rank sum). Error bars are standard error of the mean (SEM).

D. Schematic showing the injection of optogenetic viral construct into AD/AV of the anterior thalamus (see Methods).

E. Left: schematic showing the target recording region of retrosplenial cortex. Top right: DIC and EYFP fluorescence images of the target RSG showing lamination of the thalamic axons within RSG. Bottom right: zoomed in confocal view of thalamic axons in RSG showing strongest expression in L1a followed by weaker expression in L3.

F. Schematic of optogenetic stimulation of TC axons and terminal arbors over the patched cell body.

G. Trace examples of LR (purple) and RS (blue) cell responses to the 10 Hz optogenetic pulses (see Methods) at maximum laser power. LR cell shows spiking responses, while the RS cell has small EPSPs. Both cells were held at -65 mV. Blue triangles indicate optogenetic LED pulses.

H. Optogenetic activation of thalamic axons in RSG increases the firing rate of the LR (purple) but not RS (blue) neuron in a simultaneously patched pair. Neurons were held in ACSF+picrotoxin at a constant firing rate of 10-30 Hz via a 2 s current injection, and a 1 ms optogenetic pulse was delivered 500 ms into the spike train (see Methods). Top: Raster plots for all sweeps of a representative LR (purple) and RS (blue) example. Middle: Firing trace of one sweep for that same LR and RS pair. Bottom: PSTH plots evaluating all sweeps for the same LR and RS example cells.

I. Population analysis bar graph of the spike ratio for all tested LR (n=7) and RS (n=6) cells showing a significant increase in firing rate post-LED pulse in LR cells compared to RS cells ($p = 0.0012$; Wilcoxon rank sum test). Error bars are SEM.

Table 1. Intrinsic cell properties

	LR	(n)	L3 RS	(n)	L5 RS	(n)
Postnatal age at time of recording (days)	68.78 ± 4.73	(65)	75.85 ± 7.59	(34)	90.4 ± 9.01	(35)
Resting potential (mV)	-63.83 ± 0.53	(65)	-61.91 ± 0.59	(34)	-62.37 ± 0.54	(35)
Input resistance (MΩ)	380.91 ± 19.54	(55)	157.16 ± 11.66	(30)	136.80 ± 10.64	(31)
Input capacitance (pF)	31.86 ± 0.96	(55)	90.07 ± 4.53	(30)	105.53 ± 4.67	(31)
Membrane time constant (ms)	11.55 ± 0.44	(55)	13.17 ± 0.75	(30)	13.51 ± 0.82	(31)
Action potential threshold (mV)	-40.05 ± 0.48	(65)	-37.45 ± 1.25	(34)	-38.56 ± 0.70	(35)
Action potential amplitude (mV)	60.10 ± 1.17	(65)	70.77 ± 2.22	(34)	74.07 ± 1.95	(35)
Action potential width (ms)	0.67 ± 0.02	(65)	1.05 ± 0.07	(34)	1.09 ± 0.07	(35)
Spike frequency adaptation ratio	1.26 ± 0.06	(50)	2.38 ± 0.16	(31)	2.51 ± 0.24	(29)
Latency to first spike (ms)	457.28 ± 35.02	(50)	398.88 ± 61.31	(26)	209.79 ± 51.02	(21)
Rheobase (pA)	46.10 ± 3.01	(50)	89.65 ± 8.91	(26)	132.09 ± 15.76	(21)

Values are mean ± SEM. Ns are reported individually for each intrinsic property and cell type. LR cells significantly differed from L3 RS cells on the following properties: input resistance, input capacitance, spike frequency adaptation ratio, action potential amplitude, action potential width, and rheobase ($p < 0.001$ for all comparisons). Latency to first spike was not significantly different between LR and L3 RS cells ($p = 0.3271$). LR cells differed from L5 RS cells on the following properties: input resistance, input capacitance, spike frequency adaptation ratio, action potential amplitude, action potential width, rheobase, and latency to first spike ($p < 0.001$ for all comparisons). L3 RS and L5 RS cells differed significantly on both input capacitance ($p = 0.0412$) and latency to first spike ($p = 0.0341$). Wilcoxon rank sum test was used for all statistical analyses. Exact p-values for all comparisons are reported in Table S1.

Precise overlap of anterior thalamic afferents with LR, but not RS, apical dendrites

LR neurons are morphologically distinct compared to their neighboring RS neurons (Brennan et al., 2020; Kurotani et al., 2013; Yousuf et al., 2020). Given the precise laminar pattern of anterior thalamic inputs to RSG (Fig. 1E), we next investigated the overlap between the afferent thalamic axons and the respective dendritic morphologies of reconstructed LR (n = 6) and RS (n = 5) cells (see Methods). We found that the laminar distribution of dendrites from all 6 reconstructed LR neurons strongly correlated with each other at a finer scale than even sublaminar precision, but not with RS dendrites (Figure S2 and Table S2). Similarly, such fine-grained dendritic laminar distribution from all 5 reconstructed L3 RS cells correlated with each other, but not with LR dendrites (Figure S2). This suggests that the dendritic morphology of superficial RSG pyramidal neurons, notably fine-grained lamination of dendritic arbors, is consistent within a subtype but distinct across subtypes. Apical dendrites of LR neurons were most densely localized to L1a, with basal dendrites remaining confined to L3 (Figure 2A&B). In contrast, RS apical dendrites rarely entered L1a, instead existing in the deeper half of layer 1 (L1b/c), with basal dendrites in layer 5 (L5; Figure 2A&C). Projection density analysis showed localization of AD/AV axons and terminal arbors in L1a and weakly in L3 (Figure 2A-C). Thus, dendrites of LR, but not RS, cells selectively co-localize within layers 1a and 3 with AD/AV TC axons and terminal arbors. When quantified, we found that the dendritic lamination of apical dendrites from all 6 reconstructed LR neurons was positively correlated with that of the TC arbor expression ($p < 0.001$ in each case), while 3/5 of the reconstructed RS cells were negatively correlated ($p < 0.05$ in each of the 3 cases), and the remaining 2 were not correlated with the TC arbors (Figure 2D). This anatomical colocalization of LR, but not RS, dendrites with TC axons coupled with the increase in LR, but not RS, spiking in response to TC optical stimulation indicates that the anterior thalamic-retrosplenial circuit at least partially obeys Peters' rule, which states that neuronal populations with anatomically overlapping axonal and dendritic arbors are more likely to show functional connectivity (Peters, 1979; Peters and Feldman, 1976).

To further verify this, we examined the responses of L3 LR and RS neurons to TC input across the superficial layers using a targeted optogenetic stimulation in which we optically stimulated TC arbors at L1a, the layer 1/2 boundary (L1/2), and over the cell body of the patched neuron (see Methods). When delivering 1 ms LED pulses over the three laminar locations, we indeed found that LR neurons had a significantly larger postsynaptic potential (PSP) amplitude in response to the L1a LED stimulation compared to the L1/2 stimulation, despite the possibility of some light spread in the slice ($p = 0.0189$, Wilcoxon rank sum test; Figure 2E). LED stimulation over the cell body, located in L3, resulted in a nonsignificant larger PSP response amplitude than the L1/2 stimulation ($p = 0.1813$, Wilcoxon rank sum test). Similarly, LR neurons had a significantly larger PSP amplitude in response to all three LED stimulation locations

compared to their neighboring L3 RS neurons (L1a: $p = 0.00000394$, LR $n = 46$, RS $n = 15$; L1/2: $p = 0.000000172$, LR $n = 47$, RS $n = 15$; Cell: $p = 0.00000194$, LR $n = 43$, RS $n = 15$, Wilcoxon rank sum test; Figure 2E-G). This relationship persisted when picrotoxin (50 µM) was added to the bath (Figure 2F). Similarly, when TTX (1 µM) + 4-AP (100 µM; data not shown) were added to the bath, the PSP amplitude of LR neurons was again significantly larger than that of RS neurons in response to L1a LED stimulation ($p = 0.035$, Wilcoxon rank sum test; LR $n = 6$, RS $n = 7$). Thus, the connectivity between anterior thalamic TC arbors and L3 principal neurons in RSG highlights a circuit that depends on the precise sublaminar organization of both local principal cell dendrites and incoming thalamocortical axons. This demonstrates how LR neurons are uniquely adapted to respond to incoming inputs from head direction cells in the anterior thalamus because their apical dendrites precisely overlap with the dense thalamic axons in the uppermost sublamina of L1 (L1a).

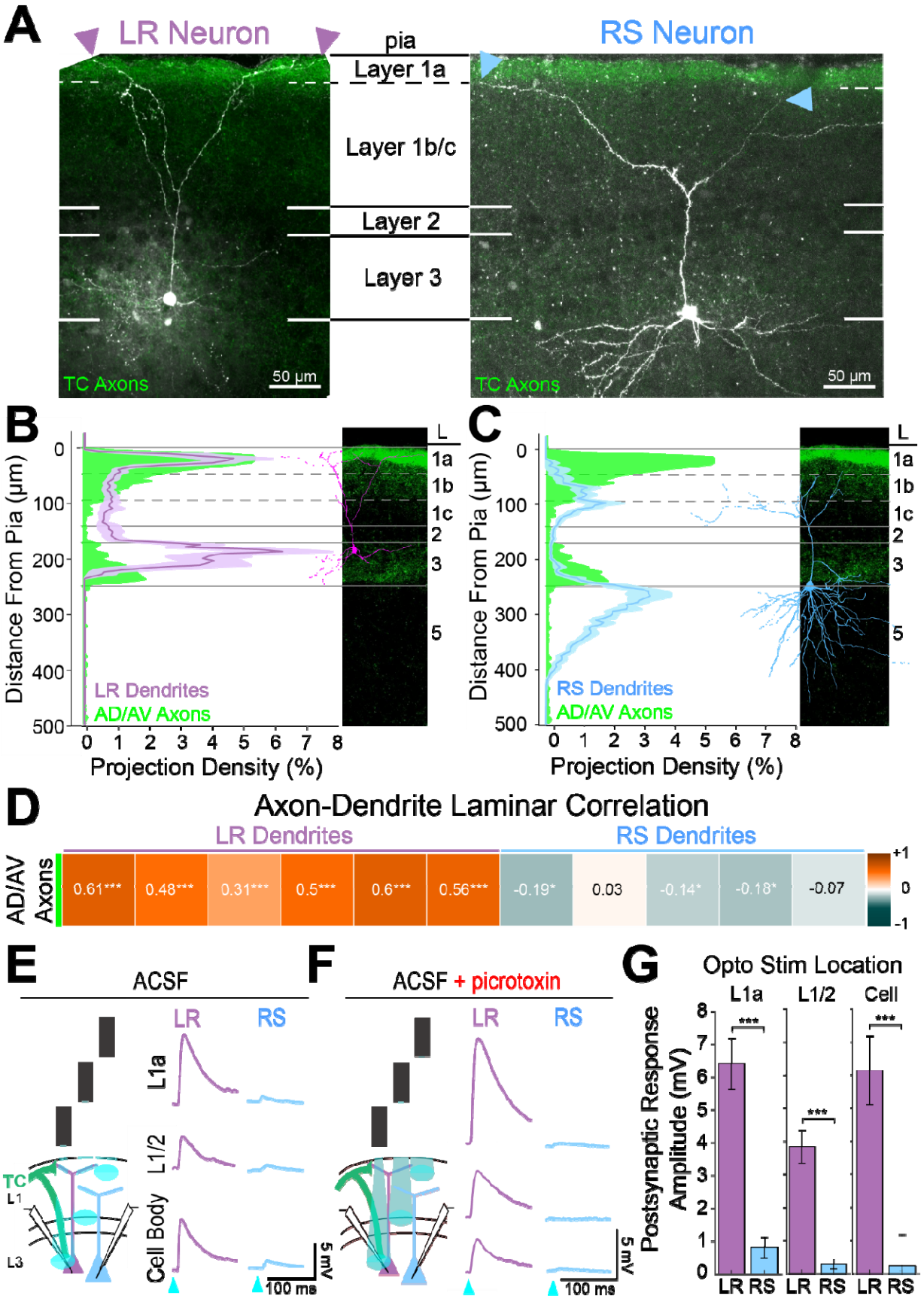
A
LR Neuron
RS Neuron
pia
Layer 1a
Layer 1b/c
Layer 2
Layer 3
TC Axons
50 µm
B
C
Distance From Pia (µm)
Projection Density (%)
LR Dendrites
AD/AV Axons
RS Dendrites
L
1a
1b
1c
2
3
5
D
Axon-Dendrite Laminar Correlation
LR Dendrites
RS Dendrites
AD/AV Axons
0.61*** 0.48*** 0.31*** 0.5*** 0.6*** 0.56*** -0.19* 0.03 -0.14* -0.18* -0.07
+1
0
-1
E
ACSF
F
ACSF + picrotoxin
LR
RS
L1a
L1/2
Cell Body
TC
L1
L3
5 mV
100 ms
G
Opto Stim Location
L1a
L1/2
Cell
Postsynaptic Response Amplitude (mV)
LR RS LR RS LR RS

Figure 2. Thalamic control of LR neurons is explained by precise convergence of LR dendrites with anterior thalamic axons in layer 1a of granular retrosplenial cortex.

- ***A.*** Fluorescent images of filled LR (left) and RS (right) neurons in a slice with eYFP-expressing AD/AV thalamic axons and terminal arbors (green). Layers are denoted by white lines, and arrows demarcate edges of apical tuft. Scale bar indicates 50 µm.
- ***B.*** Projection density plot showing density of LR dendrites (n=6; mean ± SEM shaded) in purple and density of AD/AV axon expression in green plotted from distance to the midline (µm). Right shows confocal image of anterior thalamic expression and the reconstruction of a representative LR neuron.
- ***C.*** Same as ***B*** for RS dendrites (n=5) in blue.
- ***D.*** Heatmap showing the correlation between the 6 LR and 5 RS cells' dendritic locations and retrosplenial AD/AV axonal and terminal arbor locations. LR dendrites are significantly positively correlated with AD/AV axons ($p < 0.001$ for all), signifying an overlap in laminar location. RS dendrites are either uncorrelated or significantly negatively correlated ($p < 0.05$) with AD/AV axons, signifying no overlap in laminar location. Exact p-values for all comparisons are reported in Table S2.
- ***E.*** Left: Schematic of lamination-targeted optogenetic stimulation (see Methods) conducted in standard ACSF. Right: Example traces of a representative LR (purple) and RS (blue) neuron same-slice sequential pair showing EPSP responses to optogenetic activation of AD/AV axons at the varying laminar locations of LED-based stimulation. Blue arrow marks LED-based optogenetic pulse. Note the larger response of the LR cell compared to the RS cell at all stimulation locations. Cells were held at -65 mV.
- ***F.*** Left: Schematic of lamination-targeted optogenetic stimulation (see Methods) conducted in ACSF with picrotoxin (50 µM) in the bath. Right: Example traces of representative LR (purple) and RS (blue) neuron pair showing EPSP responses to optogenetic activation of AD/AV axons at the varying laminar locations of LED-based stimulation. Blue arrow marks LED-based optogenetic pulse. Note the larger response of the LR cell compared to the RS cell at all stimulation locations. Cells were held at -65 mV.
- ***G.*** Bar graphs of population analysis for LR and RS postsynaptic response amplitudes to the LED-based optogenetic stimulations at L1a, L1/2, and cell body locations. LR cells have significantly larger responses than RS cells at all LED-based stimulation locations (L1a: $p = 0.00000394$, LR $n = 46$, RS $n = 15$; L1/2: $p = 0.000000172$, LR $n = 47$, RS $n = 15$; Cell: $p = 0.00000194$, LR $n = 43$, RS $n = 15$; Wilcoxon rank sum test), with the largest response occurring at L1a and smallest at L1/2 boundary. Error bars are SEM.

Anterior thalamic inputs to LR, but not RS, neurons show synaptic depression. Layer 3 LR and RS neurons also displayed clear differences in short term synaptic dynamics in response to TC input in both control and TTX 4-AP conditions, with LR neurons exhibiting depression while RS neurons showed weak initial facilitation ($p = 0.0037$, Wilcoxon rank sum test; Figure 3A-C). The RS cell response to TC inputs in RSG was similar to responses to anterior thalamic input in other regions of the cortex, including the cingulate and prefrontal cortices where superficial RS neurons also show weak facilitation (Figure 3D; Cruikshank et al., 2012). TC core input to sensory cortices leads to short-term synaptic depression in deep layer RS neurons that is more profound than that seen in RSG LR cells in response to matrix input (Figure 3C&D, Cruikshank et al., 2012).

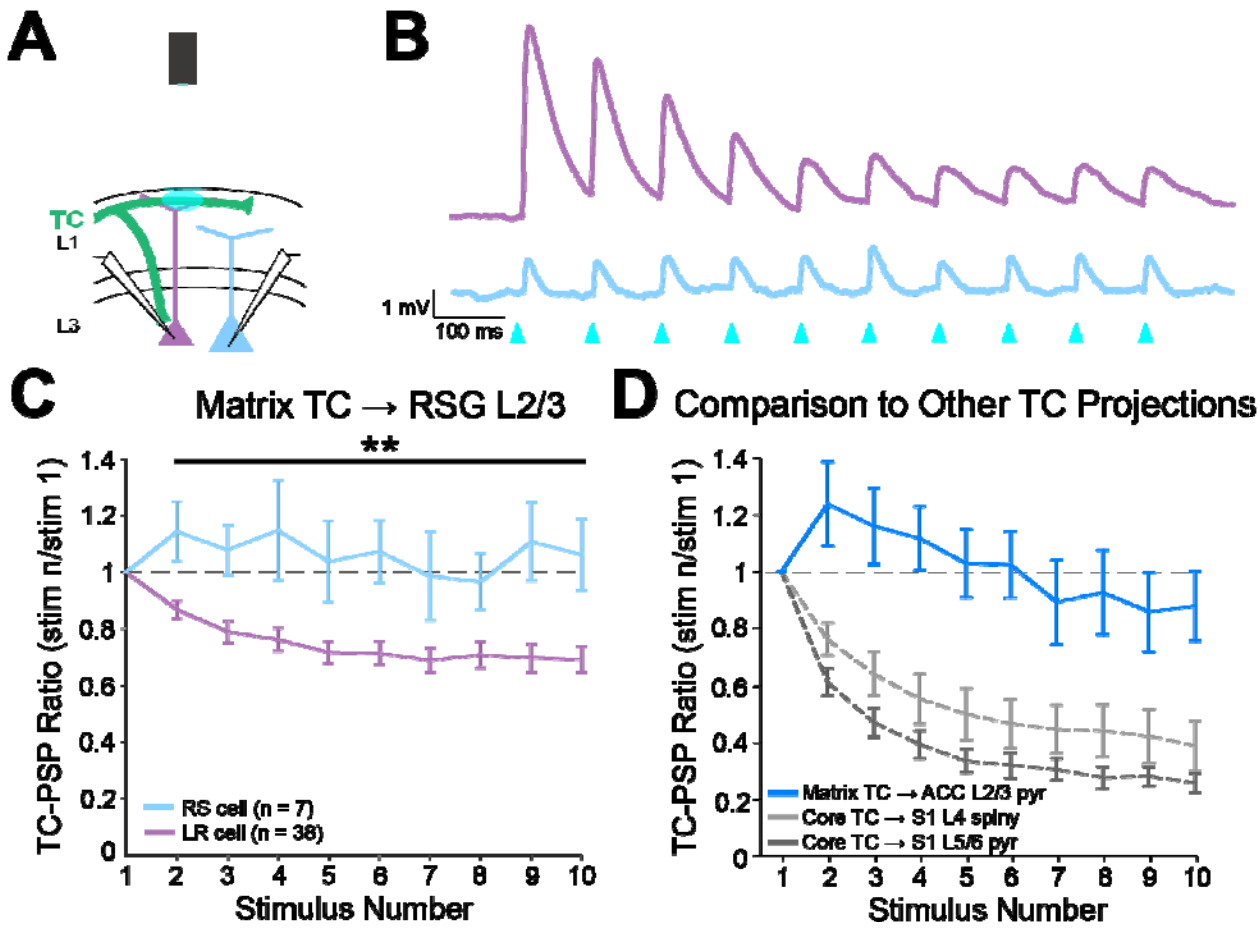

Figure 3. Short-term depression in retrosplenial LR, but not RS, neurons in response to anterior thalamic input.

- ***A.*** Schematic showing LED stimulation at layer 1a and a paired-patch LR and RS neuron.
- ***B.*** Trace example of a same-slice sequential LR (purple) and RS (blue) neuron pair showing responses to a 10 Hz train of 1 ms wide optogenetic LED pulses. Blue triangles indicate each LED pulse. Note the modest depression exhibited in the LR neuron response amplitudes, while RS neuron response amplitudes remain more constant. Cells were held at -65 mV.
- ***C.*** Group synaptic dynamics for LR (n = 38) and RS (n = 7) neurons in response to 10 Hz optical stimulation of TC arbors at L1a. LR neurons show short-term depression, while RS cells show neither depression nor facilitation. Black line indicates significant difference between LR and RS PSP ratios for pulses 2-10 (**p = 0.0037; Wilcoxon rank sum). Error bars are SEM.
- ***D.*** Previously published group synaptic dynamics, also in response to optical 10 Hz stimulation (reproduced with modified annotations from Cruikshank et al., 2012). L2/3 RS cells in anterior cingulate (ACC; n = 11) also show a lack of short-term synaptic depression in response to TC matrix input. Thus, the short-term dynamics of RSG and ACC RS cell response to anterior thalamic input is consistent across cortical regions. Primary somatosensory cortex (S1) pyramidal neurons exhibit strong short-term synaptic depression in response to core TC input. Error bars are SEM. (Cruikshank et al., 2012).

Synaptic depression of anterior thalamic input to LR neurons optimizes lower latency encoding of head direction information

Given the somewhat surprising depressing nature of anterior thalamic synapses onto LR neurons (compared to the RSG and ACC , we next sought to understand its computational implication with regard to the processing of incoming head direction inputs, particularly as it contrasts with the previously-reported facilitating input from the subiculum (Yamawaki et al., 2019a), another known source of spatial input to LR cells (Figure S3; Nitzan et al., 2020; Yamawaki et al., 2019a). Using a morphologically realistic model of retrosplenial LR cells (Brennan et al., 2020), we investigated how the short-term synaptic dynamics impact the processing of depressing versus facilitating inputs by LR neurons. Utilizing the short-term-plasticity framework of Tsodyks et al (Tsodyks et al., 1998; Tsodyks and Wu, 2013), we input Poisson spike trains at a range of input frequencies to the model LR cells (Figure 4A). We normalized the net charge across inputs, such that the inputs only differed in their short-term-plasticity (see Methods & Figure S4A&B). Since the LR neuron has a late-spiking current attributed to Kv1 expression (Brennan et al., 2020), we provided the synaptic input either early or late to simultaneously study the impact of the late-spiking current on depressing versus facilitating synaptic integration (Figure 4B). We found that over a broad range of input frequencies, depressing synapses reliably led to faster responses (reduced response latency) in comparison to facilitating synapses (Figure 4C, E). This was true whether the input was delivered early or late (Figure 4E, 4G) and whether the input was to basal or apical dendrites (data not shown). The size of the latency improvement increased with input frequency, including a large, significant benefit for depressing versus facilitating synapses at the ~80-120 Hz frequency range at which anterior thalamic head direction cells are known to fire during navigation *in vivo* (Peyrache et al., 2015; Tsanov et al., 2011). We also found that at higher input frequencies, facilitating synapses tended to produce a significantly greater number of output spikes (Figures 4D, 4F). Since the current waveforms were charge matched, we infer that this difference can be attributed to intrinsic LR dynamics. We hypothesized that facilitating synapses are more efficacious for a rate code in this scenario because afterhyperpolarization following individual spikes deniactivates the Kv1 current (Figure 4B), resulting in a context where the magnitude of the current pulse required to trigger further spiking increases; this increase is then subsequently better overcome by larger facilitated EPSCs than by smaller depressed EPSCs. Consistent with this hypothesis, we observed that the magnitude of the advantage of STF over STD is proportional to the conductance of the Kv1 current (early spiking window: $R^2 = 0.9$, $p = 2.88e-08$; late-spiking window: $R^2 = 0.82$, $p = 1.81e-06$; Figure 4H&I). Overall, the synaptic dynamics of the inputs to LR neurons are thus better suited for temporal latency coding of thalamic directional inputs but a rate code for dorsal subicular distance-related inputs, such as those likely to be provided by bursty boundary vector cells in the dorsal subiculum (Bicanski and Burgess, 2020; Lever et al., 2009; Simonnet and Brecht, 2019; Stewart et al., 2014).

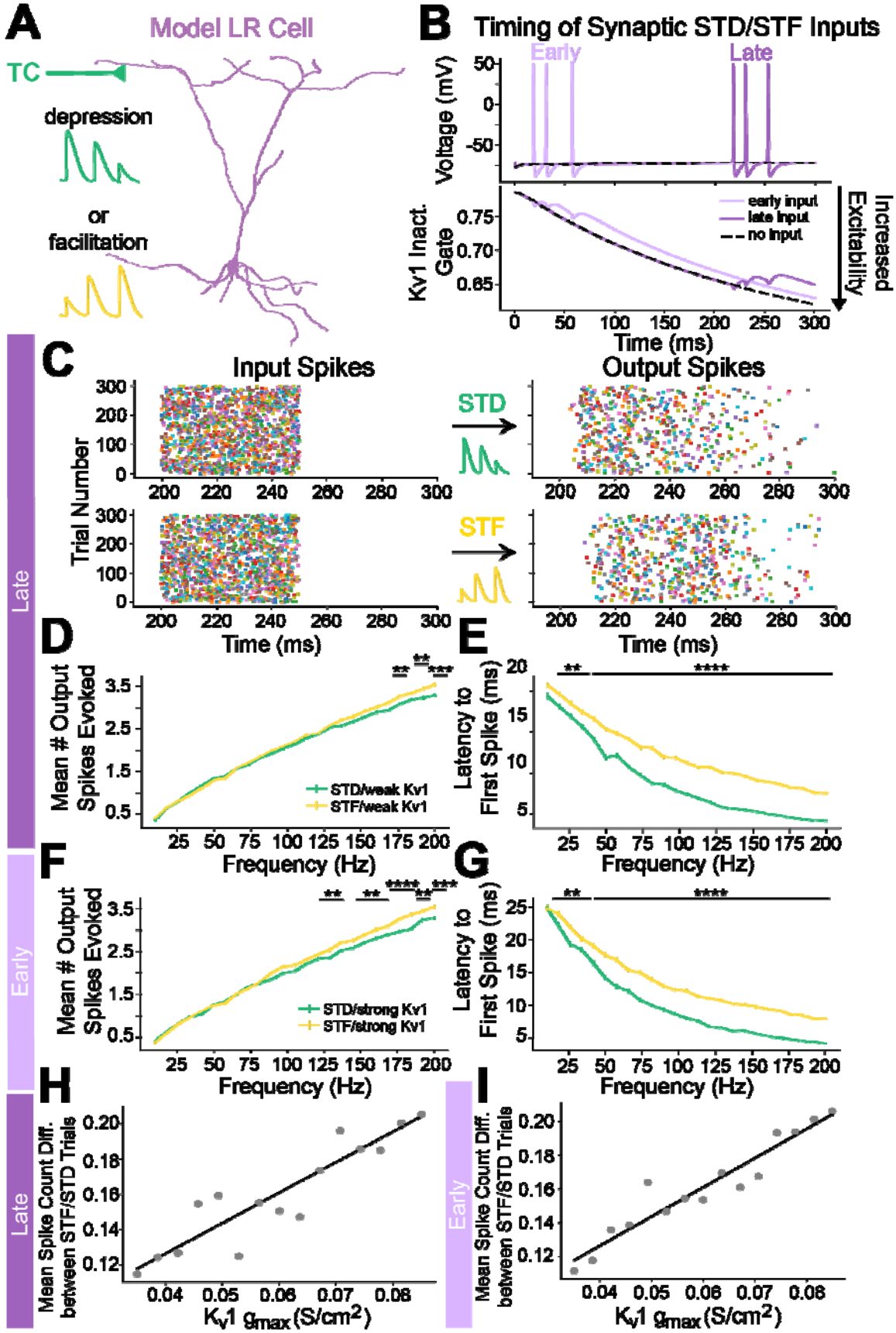
A
Model LR Cell
TC
depression
or
facilitation
B
Timing of Synaptic STD/STF Inputs
Early
Late
Voltage (mV)
Kv1 Inact. Gate
early input
late input
no input
Increased Excitability
Time (ms)
C
Input Spikes
Output Spikes
STD
STF
Trial Number
Time (ms)
D
Mean # Output Spikes Evoked
STD/weak Kv1
STF/weak Kv1
Frequency (Hz)
E
Latency to First Spike (ms)
Frequency (Hz)
F
Mean # Output Spikes Evoked
STD/strong Kv1
STF/strong Kv1
Frequency (Hz)
G
Latency to First Spike (ms)
Frequency (Hz)
H
Mean Spike Count Diff. between STF/STD Trials
Kv1 gmax (S/cm2)
I
Mean Spike Count Diff. between STF/STD Trials
Kv1 gmax (S/cm2)
Late
Early

Figure 4. Synaptic depression of LR input reduces response latency over a wide frequency range at a slight cost in response reliability.

- ***A.*** Morphologically realistic model of an LR cell receiving depressing (STD; green) and facilitating (STF; yellow) input to its apical dendrites.
- ***B.*** Top: inputs to the LR model are provided in two distinct 50 ms spiking windows. Bottom: the spiking window distinction captures some of the variability in the Kv1 current, with early input arriving in the context of a stronger Kv1 current (during which the cell is less excitable) and late input arriving in the context of a weaker Kv1 current (during which the cell is more excitable).
- ***C.*** Raster plot of Poisson spike trains input to synapses exhibiting STD and STF, respectively, showing visibly decreased response latency in the STD case.
- ***D.*** Under late input conditions, STF synapses tend to evoke more output spikes than STD synapses, especially at higher frequencies ($p = 0.0076$; Kruskal-Wallis test).
- ***E.*** Under late input conditions, and under a broad range of input frequencies, STD synapses reliably produce significantly lower latency responses than STF synapses ($p = \sim 0.0$; Kruskal-Wallis test).
- ***F.*** Same as ***D*** but for early input conditions.
- ***G.*** Same as ***E*** but for early input conditions.
- ***H.*** Maximum conductance of the Kv1 current correlates with size of the observed spiking advantage enjoyed by STF synapses over STD synapses in trials with late input conditions ($R^2 = 0.82$; $p=1.81e-06$, Wald test).
- ***I.*** Same as H but for early input conditions ($R^2 = 0.90$; $p=2.88e-08$, Wald test)

Claustrum selectively controls retrosplenial RS cells while avoiding LR cells

Another main source of subcortical input to RSG is the claustrum (CLA; van Groen and Wyss, 2003, 1990), which is thought to be involved in both regulating correlated signals within the cortex (Kim et al., 2016; Smith et al., 2012; Smythies et al., 2012) and fear conditioning (Cho et al., 2017; Ipser et al., 2013). While claustrocortical (ClaC) inputs have been shown to exhibit varying laminar targets across cortical areas (Wang et al., 2017), the precise functional nature of claustral inputs to RSG have, to our knowledge, never been examined. To address this, we used ChR2-assisted circuit mapping to examine CLA inputs to RSG LR and RS neurons and compared these projections to RSG thalamic inputs. Using dual injections consisting of ChR2 injected into CLA and an EYFP tag into AD/AV (Figure 5A), we found that TC and CLA axons and terminals have distinct and non-overlapping lamination within RSG, such that superficial TC arbors exist most strongly in layers 1a and 3, while CLA arbors exist in layers 1b/c, 2, and 5 (Figure 5B&C). Dendritic lamination plots of LR and RS dendrites and projection density plots of CLA axons and terminal arbors show that RS, but not LR, apical dendrites anatomically overlap with CLA arbors in layers 1c and 2 (Figure 5D&E). Indeed,

quantification showed that projection density of apical dendrites from all 5 reconstructed RS neurons were positively correlated with that of CLA arbors ($p < 0.05$ in all cases), while 2/6 of the reconstructed LR neurons were negatively correlated ($p < 0.05$) and the remaining 4 uncorrelated with CLA arbors (Figure 5F). Using the same targeted optogenetic stimulation approach (Figure 5G; see Methods), we found that RS neurons have significantly larger responses to CLA input compared to LR neurons at all laminar LED stimulation locations (L1a: $p = 0.0037$, LR $n = 11$, RS $n = 6$; L1/2: $p = 0.000239$, LR $n = 12$, RS $n = 8$; Cell: $p = 0.00071$, LR $n = 14$, RS $n = 6$; Wilcoxon rank sum test; Figure 5H&I). Similar preliminary results were seen with corticocortical (CC) projections to RSG from the anterior cingulate (ACC), with the ACC axons avoiding L1a and targeting L1b/c instead, overlapping with RS but not LR apical dendritic tufts (Figure S5A-C). This led to increased PSP responses of RS cells compared to LR cells in response to ACC input (Figure S5D&E). Contralateral projections to RSG from the opposite hemisphere exhibit the same lamination of axons and terminal arbors (Figure S6) and are thus also likely to evoke the same cell-type-specific response patterns. Thus, both claustrocortical and corticocortical inputs to RSG are targeted towards RS apical dendrites in lower L1 (L1b/c), whereas thalamocortical inputs preferentially target the apical dendrites of LR cells in upper L1 (L1a). This indicates that parallel circuits in RSG process TC versus ClaC, and potentially also CC, information and this parallel processing is enabled by precise sublaminar organization of neighboring layer 3 principal cell apical dendrites and afferent axons and terminal arbors.

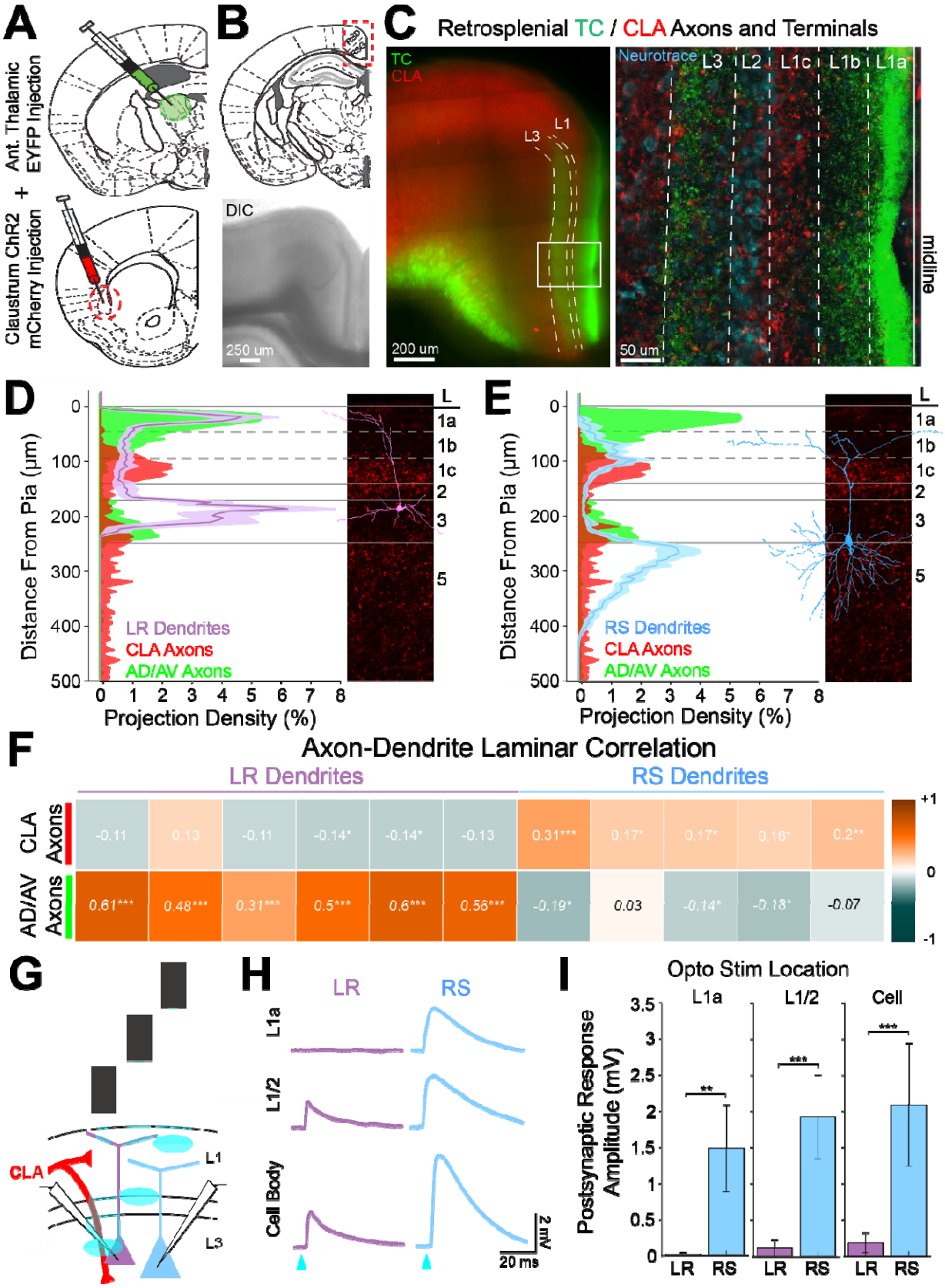
A
Ant. Thalamic EYFP Injection
+
Claustrum ChR2 mCherry Injection
B
DIC
250 um
C
Retrosplenial TC / CLA Axons and Terminals
TC
CLA
L1
L3
200 um
Neurotrace
L3
L2
L1c
L1b
L1a
midline
50 um
D
Distance From Pia (µm)
Projection Density (%)
LR Dendrites
CLA Axons
AD/AV Axons
L
1a
1b
1c
2
3
5
E
RS Dendrites
CLA Axons
AD/AV Axons
F
Axon-Dendrite Laminar Correlation
LR Dendrites
RS Dendrites
CLA Axons
AD/AV Axons
-0.11
0.13
-0.11
-0.14*
-0.14*
-0.13
0.31***
0.17*
0.17*
0.16*
0.2**
0.61***
0.48***
0.31***
0.5***
0.6***
0.56***
-0.19*
0.03
-0.14*
-0.18*
-0.07
+1
0
-1
G
CLA
L1
L3
H
LR
RS
L1a
L1/2
Cell Body
2 mV
20 ms
I
Opto Stim Location
L1a
L1/2
Cell
Postsynaptic Response Amplitude (mV)
LR
RS

Figure 5. Claustrocortical inputs to RSG result in significantly stronger activation of RS neurons compared to LR neurons, consistent with anatomical overlap of RS neuron dendrites with claustral axons.

- ***A.*** Schematic showing dual injection of the optogenetic viral construct into claustrum (CLA) and a fluorescent tag into AD/AV (see Methods).
- ***B.*** Top: Schematic of the target recording region, RSG. Bottom: DIC image of the RSG brain slice.
- ***C.*** Left: Epiflorescent image of the viral expression in the RSG brain slice. Red represents ClaC axons and terminals, and green represents AD/AV axons and terminals. Right: Zoomed in confocal image of the superficial layers of RSG, showing the brightest expression of red CLA axons in layers 1c, 2, and 5, and brightest expression of green AD/AV axons in layers 1a and 3. Blue represents the fluorescent Nissl stain, NeuroTrace, for visualization of cell bodies.
- ***D.*** Projection density plot showing density of LR dendrites (n=6; mean ± SEM shaded) in purple, density of CLA axonal and terminal arbor expression in red, and density of AD/AV axonal and terminal expression in green plotted as distance from the midline (µm). Right shows confocal image of claustrum axon expression and the reconstruction of a representative LR neuron.
- ***E.*** Same as ***D*** for RS dendrites (n=5) in blue.
- ***F.*** Heatmap showing the correlation between the 6 LR and 5 RS cells' dendritic locations, claustral axon locations, and AD/AV axon locations. LR dendrites are either uncorrelated or significantly negatively correlated with CLA axons ($p < 0.05$), signifying no overlap in laminar location. RS dendrites are significantly positively correlated with CLA axons ($n = 1$: $p < 0.001$; $n = 1$: $p < 0.01$; $n = 3$: $p < 0.05$), signifying overlap in laminar location. Exact p-values for all comparisons are reported in Table S2.
- ***G.*** Schematic of lamination-targeted optogenetic stimulation (see Methods).
- ***H.*** Example traces of representative same-slice LR (purple) and RS (blue) neuron pair showing EPSP responses to optogenetic activation of CLA arbors at the varying laminar locations of LED-based stimulation in standard ACSF. Blue arrow marks LED-based optogenetic pulse. Note the larger response of the RS cell compared to the LR cell at all stimulation locations. Cells were held at -65 mV.
- ***I.*** Bar graphs of population analysis for LR and RS postsynaptic response amplitudes to the LED-based optogenetic stimulations at L1a, L1/2, and cell body locations. LR cells have significantly smaller responses than RS cells at all LED-based stimulation locations (L1a: $p = 0.0037$, LR $n = 11$, RS $n = 6$; L1/2: $p = 0.000239$, LR $n = 12$, RS $n = 8$; Cell: $p = 0.00071$, LR $n = 14$, RS $n = 6$; Wilcoxon rank sum test). Error bars are SEM.

Layer 5 RS neurons show weaker responses to anterior thalamic and stronger responses to claustral inputs compared to LR neurons

Previous studies have shown that layer 5 RS cells (L5 RS) in RSG send apical dendrites to layer 1 and respond to TC inputs (Yamawaki et al., 2019b). We recorded from L5 RS neurons to examine their dendritic morphologies and PSP responses to TC and ClaC input to compare to our LR neuron findings. We found that L5 RS apical dendrites arborize predominantly in L1b/c (overlapping substantially with CLA axonal arbors in L1; Ichinohe et al., 2008) and also, to a small extent, in L1a (partially overlapping with TC inputs in L1; Figure 6A). While L5 RS cells did often respond to LED activation of TC arbors, their PSP responses at all LED stimulation locations were

significantly smaller than those of LR neurons (L1a: $p = 0.0000176$, LR $n = 46$, L5 RS $n = 18$; L1/2: $p = 0.0000755$, LR $n = 47$, L5 RS $n = 18$; Cell: $p = 0.0000119$, LR $n = 43$, L5 RS $n = 20$; Wilcoxon rank sum test; Figure 6B-D) and were not significantly different from the L3 RS cells (L1a: $p = 0.1866$, L3 RS $n = 15$; L1/2: $p = 0.1155$, L3 RS $n = 15$; Cell: $p = 0.0711$, L3 RS $n = 15$; Wilcoxon rank sum test; Figure 6D). These results suggest that LR neurons, and not L3 or L5 RS neurons, are the predominant RSG principal cell type receiving and processing head direction inputs from the anterior thalamus.

We also found that L5 RS neurons show the same activation patterns in response to ClaC input as L3 RS neurons. Specifically, L5 RS neurons have significantly larger PSP response amplitudes at all LED stimulation locations compared to LR neurons (L1a: $p = 0.00065$, LR $n = 11$, L5 RS $n = 9$; L1/2: $p = 0.000197$, LR $n = 12$, L5 RS $n = 9$; Cell: $p = 0.000213$, LR $n = 14$, L5 RS $n = 10$; Wilcoxon rank sum test; Figure 6E-G), but do not significantly differ from L3 RS neuron responses (L1a: $p = 0.6278$, L3 RS $n = 6$; L1/2: $p = 0.6058$, L3 RS $n = 8$; Cell: $p = 0.7756$, L3 RS $n = 6$; Wilcoxon rank sum test; Figure 6G). These results suggest that the presence of distinct pyramidal cell populations within RSG facilitates simultaneous processing of converging multimodal inputs by parallel circuits. Specifically, LR neurons are intrinsically (Brennan et al., 2020) and morphologically optimally suited to receive and integrate head direction inputs from the anterior thalamus, while RS cells are better positioned to receive higher-order inputs from ClaC and corticocortical projections.

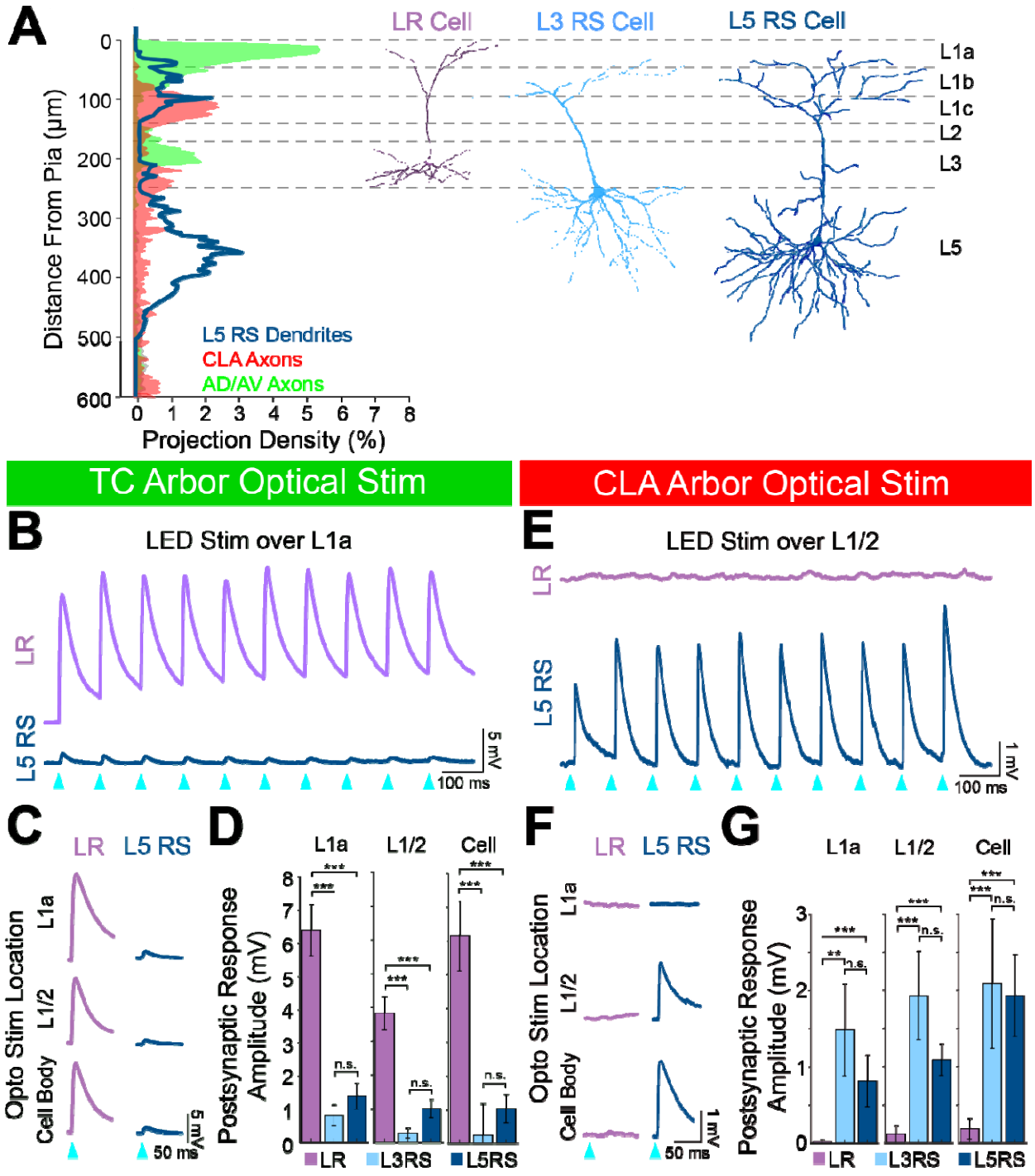

Figure 6. While morphologically distinct, RSG layer 5 RS neuron responses to TC and CLA input do not significantly differ from layer 3 RS neuron responses.

A. Left: Projection density plot of AD/AV arbors (green), CLA arbors (red), and L5 RS neuron dendrites (navy) showing an overlap with both AD/AV and CLA arbors in layer 1. Right: Representative reconstructions of LR (purple), L3 RS (blue), and L5 RS (navy) neurons aligned in the cortical layers. The small LR neuron shows an apical tuft predominantly in L1a and sparse basal dendrites in L3. The L3 RS neuron shows an apical tuft predominantly in L1b/c and basal

dendrites in L5. The large L5 RS neuron shows an apical tuft across all of L1 and basal dendrites in L5.

B. Trace example of a simultaneously patched LR (purple) and L5RS (navy) neuron pair showing responses to 10 Hz train of 1 ms wide optogenetic LED pulses in ACSF with 50 µM picrotoxin. Blue triangles indicate each LED pulse. Note the modest depression exhibited in both the LR and L5RS neuron response amplitudes. Cells were held at -65 mV.

C. Example EPSP traces of same pair as ***B*** when responding to optogenetic activation of TC arbors at the cell body, L1/2, and L1a in ACSF with 50 µM picrotoxin. Blue arrow marks LED-based optogenetic pulse. LR neuron responses are larger than L5 RS responses at all stimulation locations. Cells were held at -65 mV.

D. Bar graphs of the population data for LR, L3 RS, and L5 RS neuron responses to TC input. LR responses are significantly larger than both L3 RS and L5 RS at each LED stimulation location, while L3 RS and L5 RS responses do not differ. L1a: LR n = 46, L5 RS n = 18, L3 RS n = 15, LR v L5 RS p = 0.0000176, L3 RS v L5 RS p = 0.1866; L1/2: LR n = 47, L5 RS n = 18, L3 RS n = 15, LR v L5 RS p = 0.0000755, L3 RS v L5 RS p = 0.1155; Cell: LR n = 43, L5 RS n = 20, L3 RS n = 15, LR v L5 RS p = 0.0000119, L3 RS v L5 RS p = 0.0711; Wilcoxon rank sum test. Error bars are SEM.

E. Trace example of a same-slice sequential pair of LR (purple) and L5RS (navy) neurons showing responses to 10 Hz train of 1 ms wide optogenetic LED pulses in ACSF with 50 µM picrotoxin. Blue triangles indicate each LED pulse. Cells were held at -65 mV.

F. Example EPSP traces of the sequential pair as in ***E*** when responding to optogenetic activation of CLA arbors at the cell body, L1/2, and L1a in ACSF with 50 µM picrotoxin. Blue arrow marks LED-based optogenetic pulse. L5 RS neuron responses are larger than LR responses at all stimulation locations. Cells were held at -65 mV.

G. Bar graphs of the population data for LR, L3 RS, and L5 RS neuron responses to CLA input. LR responses are significantly smaller than both L3 RS and L5 RS at each LED stimulation location, while L3 RS and L5 RS responses do not differ. L1a: LR n = 11, L5 RS n = 9, L3 RS n = 6, LR v L5 RS p = 0.00065, L3 RS v L5 RS p = 0.6278; L1/2: LR n = 12, L5 RS n = 9, L3 RS n = 8, LR v L5 RS p = 0.000197, L3 RS v L5 RS p = 0.6058; Cell: LR n = 14, L5 RS n = 10, L3 RS n = 6, LR v L5 RS p = 0.000213, L3 RS v L5 RS p = 0.7756; Wilcoxon rank sum test. Error bars are SEM.

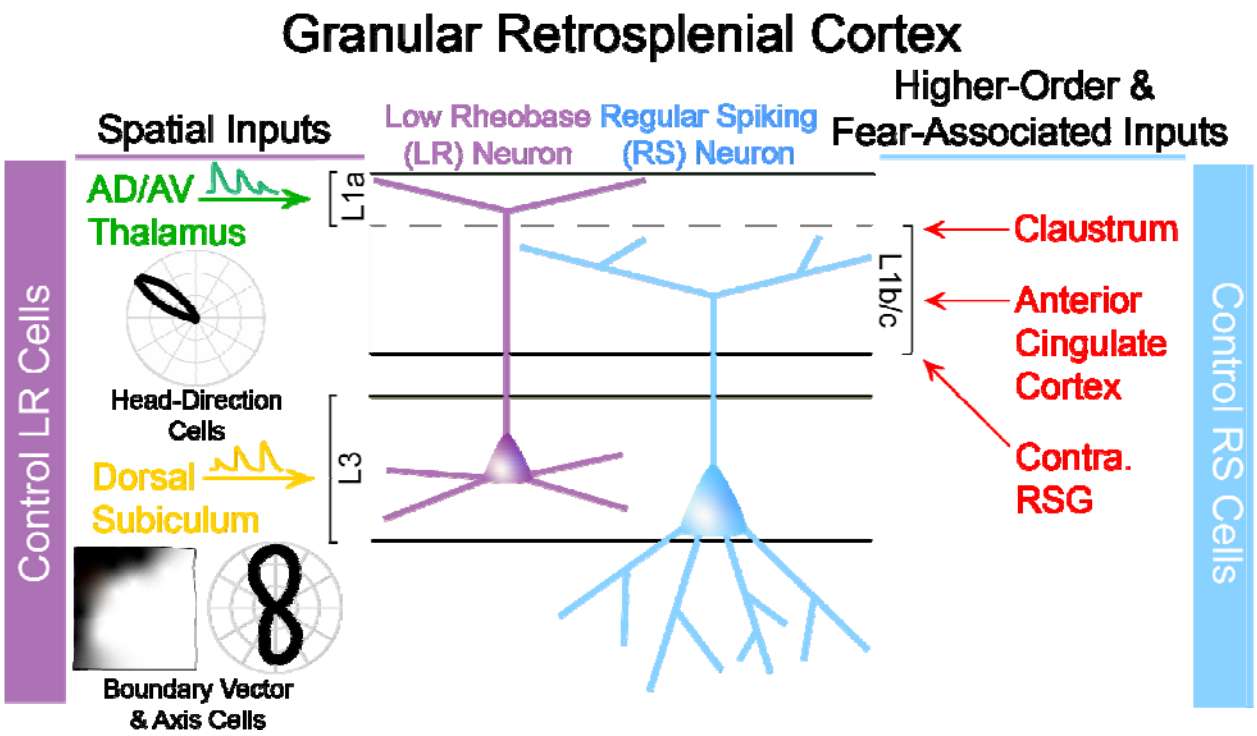

Figure 7. LR neurons are uniquely positioned to selectively integrate direction and distance information, while RS neurons may process higher-order and fear-related information. Summary figure of the main findings. Middle panel shows schematics of LR and RS neurons and their placement in the superficial layers of RSG. Left panel shows depressing head direction inputs from anterior thalamus and facilitating boundary vector and/or axis cell inputs from dorsal subiculum overlapping with LR dendrites in L1a and L3 but not with RS dendrites. Right panel shows higher-order and fear-related inputs from claustrum, anterior cingulate cortex, and contralateral RSG overlapping with RS apical dendrites, but not LR dendrites. This precise organization of LR and RS dendrites and incoming spatial versus higher-order information facilitates a parallel circuit in which LR neurons are optimized to selectively integrate direction and distance information, supporting the navigational functions of the RSC, while RS neurons are optimized to encode higher-order inputs, potentially supporting the fear-associated functions of the RSC.

DISCUSSION

We have established a circuit that facilitates parallel processing of anterior thalamic head direction input and claustrocortical higher-order/fear-related input within the superficial granular retrosplenial cortex. LR neurons receive significantly stronger activation from anterior thalamic neurons compared to both layer 3 and layer 5 RS cells (Figures 1, 2, & 6) due to the precise overlap of their apical dendrites with TC axons and terminal arbors in layer 1a (Figures 2 & 6). Conversely, RS cells receive stronger input from ClaC axons and terminal arbors that overlap with the RS cells' apical tufts in L1b/c (Figures 3 & 6). These distinct parallel circuits, facilitated by the unique intrinsic and morphological features of neighboring principal neuron subtypes, suggest that LR cells are precisely suited to selectively integrate spatial information, which is one of the key computational functions of the RSC, while RS cells may serve to process higher-order inputs that play an important role in facilitating the fear-conditioning functions of the RSC (Figure 7).

The distinct electrophysiological properties of LR neurons, specifically, play an integral role in the RSC's unique capacity to process anterior thalamic head direction inputs. We have previously reported that the low rheobase and lack of spike frequency adaption of these neurons are their defining computational features (Brennan et al., 2020). For this reason, we refer to them as low-rheobase (LR) neurons. They have also been called late-spiking (LS) neurons (Kurotani et al., 2013; Yousuf et al., 2020), but we believe this name is not optimal for several reasons. First, latency to first spike does not significantly differ between LR neurons and their neighboring superficial RS neurons within RSG (Figure 1, Table 1, Figure S1; Brennan et al., 2020), as RS neurons also exhibit a substantial delay to first spike, likely due to increased Kv1.1 or 1.2 channel expression in this region compared to other cortical areas (Kurotani et al., 2013). Additionally, the inhibitory fast-spiking (FS) cells in this region similarly exhibit a large delay to first spike that does not differ significantly from that of LR neurons, so late-spiking is not a distinctive feature of LR neurons nor excitatory neurons in this region. Second, the name "late-spiking (LS) neuron" is already the accepted and widely used nomenclature referring to a distinct subtype of inhibitory interneuron, the neurogliaform cells that are located throughout the cortical layers in many regions of the brain, including within layer 1 of RSG (Cruikshank et al., 2012; Hestrin and Armstrong, 1996; Kawaguchi and Kubota, 1997; Overstreet-Wadiche and McBain, 2015). Thus, the defining computational feature of the small, pyramidal cells in L2/3 of the RSG is their low rheobase, and this nomenclature serves to provide an unambiguous name for these hyperexcitable cells.

The small, excitable LR cells are unique among pyramidal cells not just in RSG, but also across the cortex, with no evidence, to our knowledge, for such cells in any other cortical regions (Holmgren et al., 2003; Jiang et al., 2015; Kurotani et al., 2013; Wyss et al., 1990). The precise overlap of LR apical dendrites with AD/AV TC inputs due to their

distinct morphology coupled with their unique physiological properties that support persistent information encoding indicates that they are specially adapted to process sustained head direction inputs (Brennan et al., 2020). Previous work has reported TC-evoked responses in layer 5 RS neurons at their apical dendrites (Yamawaki et al., 2019b), with some variation in the magnitude of responses across cells. Our results reproduce these observations. Layer 5 is not a homogenous layer, often divided into sublayers 5A and 5B (Geijo-barrientos et al., 2019; Sempere-Ferràndez et al., 2018; Sigwald et al., 2020; Sripanidkulchai and Wyss, 1987; Yamawaki et al., 2016a), and contains a variety of pyramidal cells, including the thin-tufted and thick-tufted neurons whose apical dendritic branches may show different sublaminar targeting in layer 1 (Galloni et al., 2020; Wyss et al., 1990). Further work is needed to determine whether any particular subtype of layer 5 pyramidal neurons may exhibit substantial TC-evoked responses, but our results, reporting significantly larger responses to TC input by LR neurons, suggest LR cells are the predominant spatial information-encoding subtype within RSG. The dorsal subiculum, which serves to transmit allocentric spatial information, including axis cell and boundary vector signals (Lever et al., 2009; Derdikman, 2009; Olson et al., 2017; Simonnet and Brecht, 2019; Bicanski & Burgess, 2020), also precisely targets LR neurons via projections localized to layer 3 of RSG (Figure S3; Nitzan et al., 2020; Yamawaki et al., 2019a). These inputs overlap with LR cell bodies and basal dendrites and have been shown to evoke larger excitatory postsynaptic currents in superficial compared to layer 5 pyramidal neurons (Figure S3; Nitzan et al., 2020; Yamawaki et al., 2019a). Thus, the distinct morphology and intrinsic properties of LR neurons make them ideally suited to integrate head direction input from the thalamus and spatial inputs from the hippocampal formation via the dorsal subiculum. Indeed, this integration of various types of directional and distance information is often stated as the key computational function of the retrosplenial cortex as a whole (Burgess et al., 2001; Byrne et al., 2007; Epstein, 2008; Ichinohe et al., 2003; Maguire, 2001), further highlighting the defining role that LR cells are likely to serve in the RSG. These LR neurons do not synapse onto neighboring neurons, instead sending their axons into the corpus callosum (Brennan et al., 2020) and may serve to influence activity of the contralateral RSC (Geijo-barrientos et al., 2019; Sempere-Ferràndez et al., 2018). Lamination of these contralateral projections suggests targeting of other retrosplenial neurons, but not contralateral LR cells, as terminal arbors distinctly avoid layers 1a and 3 where LR dendrites are predominantly located (Figure S6). Instead, electrical stimulation of one hemisphere results in recruitment of feedforward inhibition in the homotypic contralateral region, and imaging indicates this is indeed mediated by superficial pyramidal neurons dysgranular retrosplenial cortex (Geijo-barrientos et al., 2019; Sempere-Ferràndez et al., 2018), but remains to be tested in RSG. Thus, activation of LR neurons by head direction inputs in one hemisphere may lead to the silencing of LR neurons in the contralateral hemisphere via feedforward inhibition, but the functional impact of such contralateral suppression in RSG remains to be understood.

In contrast to AD/AV inputs to RSG, claustrocortical (ClaC) axons and terminal arbors avoid laminar overlap with LR apical dendrites, instead projecting to L1b/c and L5, correlating with RS apical and basal dendrites (Figures 5&6). The claustrum is believed to coordinate correlated signaling between related regions through its widespread connectivity and feedback signaling from cortical and subcortical targets (Kim et al., 2016; Smith et al., 2012; Smythies et al., 2012) and serves as a prominent input of higher-order signals to the cortex and the RSC (Wang et al., 2017). In addition, the CLA is also heavily implicated in fear conditioning (Cho et al., 2017; Ipser et al., 2013). The dorsal and ventral nuclei of the CLA facilitate emergence of the emotional state of fear (Vakolyuk et al., 1980), and increased claustral activity is reported in human phobia (Ipser et al., 2013) and animal shock and fear conditioning studies (Cho et al., 2017; Vakolyuk et al., 1980; Vetere et al., 2017). Notably, the CLA also integrates converging inputs from various fear-related regions, including the ACC (Wang et al., 2017; Zingg et al., 2018), PFC (Wang et al., 2017), entorhinal cortex (Kitanishi and Matsuo, 2017), and amygdala (Majak et al., 2002), and projects unilaterally to the RSC (Zingg et al., 2018). Surprisingly, the RSC is one of the few regions that does not send reciprocal connections to the CLA; instead, claustral cells that project to RSC receive dense synaptic connections from other fear-related limbic areas (Zingg et al., 2018). This suggests precise modulation and coordination of fear signals converging in RSC, establishing retrosplenial circuits as a crucial computational endpoint in certain fear-conditioning behaviors. Indeed, studies have shown that the RSC, and not the amygdala, is necessary for trace fear-conditioning and extinction (Kwapis et al., 2014), and retrosplenial damage results in impaired fear memory (Sigwald et al., 2020; Todd et al., 2017). The ACC is similarly implicated in trace fear-conditioning (Han et al., 2003; Steenland et al., 2012; Vetere et al., 2011; Zhao et al., 2006), and its interactions with the RSC may partly facilitate the encoding and early retrieval of novel fear associations (Corcoran et al., 2016). ClaC and ACC axons and terminal arbors in RSG show similar lamination, overlapping with RS dendrites in L1b/c and L5, while distinctly avoiding LR dendrites in L1a and L3 (Figure 5, Figure S5). This precise sublaminar organization results in control of RS, but not LR, neurons by CLA and ACC signaling, suggesting that RS neurons may be the predominant cell type underlying the retrosplenial role in fear processing. Indeed, elimination of so-called “layer 4” RS cells in RSG results in contextual fear amnesia (Sigwald et al., 2020), implying that these layer 4 RS cells, which, due to the controversial nature of the RSG layer 4 described below, may overlap with our deep layer 3 RS cells, are the key cell type facilitating contextual fear-conditioning in the RSC. Thus, the precise organization of RSG neurons and inputs facilitates the functional specification of neighboring principal neuron subtypes, with LR neurons underlying the RSC’s navigational functions and RS cells underlying its contextual fear functions.

Layer 3 consists predominantly of LR neurons, with RS cells accounting for about 10% of neurons identified in this layer (Brennan et al., 2020). Of this 10%, the vast majority are located at the boundaries of L3, closest to layer 2 and, most often, layer 4. Indeed,

of our 5 reconstructed RS neurons, 4 had at least a portion of their cell bodies at the layer 3/4 boundary. While anatomical studies report the existence of layer 4 in the granular region of RSC (van Groen and Wyss, 2003, 1990; Wyss and van Groen, 1992), no current studies to our knowledge have examined the electrophysiological properties and connections of layer 4 RSG neurons. Defining the laminar boundaries of layer 4 is particularly challenging, as all current definitions rely on anatomical observations (Ichinohe et al., 2008; Sripanidkulchai and Wyss, 1987) or expression of cholinergic molecular markers (Sripanidkulchai and Wyss, 1987). A previous study showed that in motor cortex, a region which lacks a cytoarchitecturally-defined layer 4, pyramidal neurons exhibited prototypical layer 4 circuits with connectivity patterns similar to those of other cortical areas containing a standard layer 4, such as sensory cortices (Yamawaki et al., 2014). These motor and sensory layer 4 pyramidal neurons rarely receive corticocortical inputs, instead receiving strongest inputs from core thalamic projections (Alfano and Studer, 2013; Feldmeyer et al., 2013; Yamawaki et al., 2014). This differs from our observations in RSG, with RSG neurons near the L3/4 boundary receiving significantly stronger ClaC and CC input, suggesting that our deep layer 3 RS cells are unlikely to be a separate population of layer 4 neurons. Further electrophysiological and morphological studies are needed to carefully examine the intrinsic and connectivity properties of the controversial retrosplenial layer 4 neuronal populations to clarify the definition of layer 4 in RSG.

Another important consideration within the circuits examined here is the role of feedforward inhibition. Matrix TC inputs evoke feedforward inhibition to regulate cortical signaling through both disinhibition (Anastasiades et al., 2020; Delevich et al., 2015) and the disynaptic inhibition of pyramidal neurons in the target region (Cruikshank et al., 2012; Yamawaki et al., 2019a). Indeed, anterior thalamic inputs to RSG result in both monosynaptic excitation but also disynaptic inhibition of layer 5 RS cells (Yamawaki et al., 2019b). Similarly, ClaC inputs invoke feedforward inhibition in several cortical regions, particularly through recruitment of neuropeptide Y (NPY) and, to a lesser degree, FS cells (Jackson et al., 2018), and this is thought to be a large component of the claustrum's widespread regulatory functions throughout the cortex. Future work will examine the effect of potential feedforward inhibition on the subpopulations of retrosplenial principal neurons in response to both TC and ClaC input in order to establish a thorough understanding of the circuitry facilitating retrosplenial integration of converging inputs, particularly the processing of head direction input. Long-range inhibitory signals from CA1 of the hippocampus also target apical dendrites in retrosplenial layer 1a, converging with excitatory anterior thalamic inputs, to precisely regulate these TC inputs and establish a hippocampo-thalamo-retrosplenial network (Yamawaki et al., 2019b). This fine-grained laminar overlap strongly suggests that these inhibitory signals may regulate LR responses to matrix TC input more strongly than layer 5 cells and should be investigated further, particularly in the context of integration of spatial information processing.

Our findings also highlight a framework by which other cortical regions integrate and process thalamic versus claustral inputs. Laminar dichotomies similar to those seen in RSG in this study also exist between TC and ClaC projections to other cortical regions such as the medical prefrontal cortex (Figure S7; Wang et al., 2017). While other cortical regions do not contain LR neurons, as these are specific to RSG, it is likely that apical dendritic lamination differences between varying pyramidal and inhibitory cell populations facilitate similar subtype-specific connectivity of afferent signals.

In summary, our results highlight a circuit enabled by the precise sublaminar organization of distinct neuronal subtypes and afferent arbors that can support the diverse navigational and fear-related functions of the retrosplenial cortex in parallel. LR neurons receive allocentric directional and spatial inputs from the anterior thalamus and dorsal subiculum, respectively. Thus, the unique physiological and morphological properties of the LR neuron create a cell-type within the retrosplenial cortex optimized for the integration of converging direction and distance information, a key computational function attributed to RSC. In contrast, neighboring RS neurons in RSG respond very weakly to spatial inputs, as their apical and basal dendrites distinctly avoid laminar overlap with anterior thalamic and subicular afferents. Instead, RS neurons respond to claustrocortical and anterior cingulate inputs, establishing a circuit that can serve to process higher-order and fear related signals, thus supporting the contextual fear functions attributed to RSC. How these two parallel streams of information are integrated in downstream neurons within both the ipsilateral and contralateral granular and dysgranular retrosplenial cortices is the next critical step towards a mechanistic understanding of retrosplenial computations.

ACKNOWLEDGEMENTS

We would like to thank Roger Albin and Clare Weiland for their comments on the manuscript, Vaughn Hetrick for his technical assistance, and Michael Roberts for his help with the NeuroLucida software. This work was supported by lab startup funds from the University of Michigan to OJA and partially supported by pilot funds to OJA from the NIH/NIA funded Michigan Alzheimer's Disease Research Center (5P30AG053760), and by an NSF graduate research fellowship to EKWB.

AUTHOR CONTRIBUTIONS

Conceptualization, O.J.A, E.K.W.B., I.J-C; Methodology, O.J.A., E.K.W.B., I.J-C; Investigation, E.K.W.B., I.J-C., S.P.R., S.K.; Software, S.K., S.K.S., I.J-C., E.K.W.B., O.J.A.; Formal Analysis, E.K.W.B., I.J-C., S.K.; Visualization, E.K.W.B., I.J-C., S.K., O.J.A.; Writing – Original Draft, E.K.W.B., O.J.A.; Writing – Review & Editing, O.J.A., E.K.W.B., I.J-C., S.K., S.K.S., S.P.R.; Funding Acquisition, O.J.A.; Supervision, O.J.A.

COMPETING INTERESTS

The authors declare no competing financial interest.

METHODS

All procedures and use of animals were approved by the University of Michigan Institutional Animal Care and Use Committee. The following mouse lines were used in this study: Ai14 (Jackson Laboratories, 007914; n=4), Ai32 (Jackson Laboratories, 024109; n=7), C57Bl6 wildtypes (Charles River, stock #027; n=12), CaMKIIα-Cre (Jackson Laboratories, 005359; n=2), Grp-KH288-Cre (RRID:MMRRC 037585-UCD; n=5), PV-IRES-Cre (Jackson Laboratories, 008069; n=3), and PV-IRES-Cre x Ai14 (crossed in house; n=4). Mice of both sexes between the ages of P43–P184 were included in the experiments.

Experimental procedures

Surgical procedures

Surgical anesthesia was induced via isoflurane inhalation at 4% and then maintained on a surgical anesthetic plane at 2-3% isoflurane. Upon induction, atropine was injected subcutaneously at 0.05 mg/kg. A Physitemp (Clifton, New Jersey, USA) controller monitored and maintained body temperature at 37ºC. Ophthalmic ointment was placed on the eyes. The incision site was prepared using 1:40 Nolvasan followed with isopropyl alcohol before being subcutaneously injected with 1% lidocaine. The skull was then leveled, and bregma was identified. Using a digital stereotaxic coordinate system, the following injection target sites were identified: right anterodorsal thalamic nucleus (AP = -0.6 mm, ML = +0.78 mm, DV = -2.5, -3.25 mm), right claustrum (AP = +1.25 mm, ML = +2.6 mm, DV = -3.3 mm), right dorsal subiculum (see Figure S3; AP = -3.0 mm, ML = +1.5 mm, DV = -1.5, -1.8 mm), and right anterior cingulate cortex (see Figure S5; AP = +0.3 mm, ML = +0.3 mm, DV = -0.7, -1.0 mm). Burr holes were then drilled through the skull at the identified sites, and dura was removed. Micropipettes were lowered under stereotaxic guidance into the target injection site containing the ChR2 viral construct (AAV2-EF1a-DIO-hChR2(h134R)-eYFP for GRP-Cre mice and AAV2-hsyn-ChR2(H134R)-eYFP for all other lines, UNC Gene Therapy Vector Core). For dual injection surgeries, the ChR2 viral construct was injected into the functional target, and a mCherry tag (AAV2-hsyn-mCherry) was injected into the other region for visual comparison of various afferent axonal and terminal arborizations within the same animal.

Injections of 0.5 µL total virus volume at each depth were given via picospritzer at 0.05-0.07 µL/min with a 5-minute pause between injecting the more dorsal and ventral thalamic DV coordinates. After a region was injected, there was a 10-minute period before removing the micropipette from the brain. Enrofloxacin was administered at 8.0 mg/kg after injections. Burr holes were sealed with bone wax, and the incision was closed with VetBond with antibiotic ointment placed under skin edges. Isoflurane was tapered down prior to removal. After removal from isoflurane, carprofen was

administered at 5 mg/kg. The mice were kept warm through an artificial heat source during the recovery period. Mice then recovered for 2-14 weeks post-injection before being used for slice experiments.

Slice preparation

Slices were prepared as described previously (Brennan et al., 2020). Briefly, mice were deeply anesthetized using isoflurane before decapitation. Brains were removed and placed in a carbogen-saturated ice-cold high-sucrose slicing solution within 30 seconds of decapitation. Using a Leica 1200VT or Leica 1000S vibratome, 300 µm coronal slices were cut and placed in a high-magnesium artificial cerebrospinal fluid (ACSF) solution at 32ºC. After resting in this solution for 20 minutes, the entire bath was moved to room temperature where the slices rested for the remainder of the experiment.

Whole-cell recordings

During whole-cell recordings, slices were submerged in a recording chamber with a 2 mL/minute flow of body-temperature ACSF (126 mM NaCl, 1.25 mM NaH2PO4, 26 mM NaHCO3, 3 mM KCl, 10 mM dextrose, 1.20 mM CaCl2, and 1 mM MgSO4). They were visualized using an Olympus BX51WI microscope, Olympus 60x water immersion lens, and Andor Neo sCMOS camera (Oxford Instruments, Abingdon, Oxfordshire, UK). Patch pipettes had a diameter of 2-4 µm and resistances between 2-5 MΩ. The potassium gluconate internal solution used in these experiments contained 130 mM K-gluconate, 2 mM NaCl, 4 mM KCl, 10 mM HEPES, 0.2 mM EGTA, 0.3 mM GTP-Tris, 14 mM phosphocreatine-Tris, and 4 mM ATP-Mg and had a pH of 7.25 and osmolarity of 290 mOsm.

Current-clamp recordings were conducted using the Multiclamp 700B and Digidata 1550B (Molecular Devices). Patched neurons were adjusted for series resistances and held at resting potentials between -65 mV. Recordings were not corrected post hoc for liquid junction potential. Resting membrane potential, defined as recorded potential within 30 seconds of break-in, was recorded, and cells with resting potentials more depolarized than -50 mV were not included in this study. Intrinsic neuronal properties were calculated using a set of protocols detailed below, measured with a custom MATLAB script, and verified in Clampfit. Pharmacological agents were prepared prior to experiments as outlined by the manufacturer and added to the ACSF. Agents were applied for at least 10 minutes before conducting experiments, and verification of effect was visualized (no spiking at current injections for TTX-4AP; no feedforward inhibition for picrotoxin).

Channelrhodopsin-assisted circuit mapping

Channelrhodopsin-assisted circuit mapping (CRACM) experiments (Yamawaki et al., 2016b) were conducted under the same rig set-up as described above while using a 5,500K white light-emitting diode (LED; Mightex; maximum power of 14.47 mW measured at the slice focal plane). Synaptic responses to optical stimulation of the ChR2-expressing axons were measured from postsynaptic retrosplenial neurons recorded under whole-cell current-clamp conditions.

In order to examine the effect of afferent axonal input to retrosplenial neurons, two optogenetic stimulation protocols were used. First, a targeted optogenetic stimulation approach was used to examine the distribution of afferent axons and terminal arbors across the cortical layers in which the postsynaptic retrosplenial neurons resided. The main areas of interest included layer 1a (L1a; defined as the top 1/3 of layer 1 adjacent to the midline), layer 1/2 boundary (L1/2; defined as the border between the sparse layer 1 and densely-packed layer 2), and the location of the patched cell body (all patched cells were located in layers 3 or 5). For LED-based stimulation over L1a, the objective was centered approximately 30 µm from the midline in layer 1. For LED-based stimulation over L1/2, the objective was centered over the border between L1 and L2. For LED-based stimulation over the cell body, the objective was centered on the patched cell body at its widest diameter. For LR to L5 RS comparisons, layer 5 LED-based stimulations were also conducted. The objective was centered over the cell body of the L5 neuron (in LR-L5 RS true pairs) or approximately 100 µm from the layer 3/4 boundary (in single-patched LR conditions). All LED-based stimulations were aligned in the cortical column with the patched cell body. LED intensity was kept constant at each stimulation location and was set at the minimum intensity necessary to evoke the smallest visible response when stimulating at the L1/2 location. For most cells, this L1/2 response was between 0.25-5 mV, while strongly activated cells had larger responses with the smallest possible LED intensity. All layer test optogenetic stimulation protocols consisted of a 1 second 10 Hz train of 1 ms LED pulses.

Second, a current step protocol was used to examine the effect of thalamic input on the postsynaptic retrosplenial neurons' spike trains. In this protocol, a 2 sec current step was delivered to the postsynaptic cell that elicited a 10-30 Hz spike train with a 1 ms LED pulse delivered at 500 ms into the current step. The objective for this protocol was centered directly over the cell body.

Morphological investigations and reconstructions

Cell filling and visualization

To analyze the morphology of the cells, biocytin (5mg/ml) was added to the recording solution fresh every day. Biocytin was allowed to diffuse into the cell for no less than 20 min. Shortly before removing the patch pipette from the neuron, ten current pulses (1-3nA at 1Hz) were applied to aid the diffusion process (Jiang et al., 2015). After the fill

process was complete, the patch pipette was retracted from the cell slowly to allow the membrane resealing. 1-4 cells were filled per slice, and then the slice was transferred from the recording chamber to 4% PFA for overnight fixation. The next day, slices were washed in PBS and incubated for 24-48 hours in streptavidin conjugated Alexa Fluor (488, 594 or 647) with 0.2% TritonX added to permeabilize the cells. After this incubation, slices were washed in PBS mounted on slides and cover slipped using Fluoromount-G.

Cell reconstruction

Z-stacks of each filled cell were acquired using the Leica SP5 confocal microscope with a dry 40x lens or the Zeiss Axio Image M2 confocal microscope with 20x lens. Reconstructions from z-stacks were performed using NeuroLucida software in user-guided mode. Additional reconstructions previously generated were also added to the analyses described below (Brennan et al., 2020).

Imaging of slice expression

Representative images of axonal projection to RSG were obtained from mice injected with anterograde AAV2 into AD/AV and claustrum. Slices were prepared as for electrophysiology recordings. After use, slices with well-defined RSC were fixed overnight in 4% PFA and then stained with the fluorescent Nissl stain, NeuroTrace 435-455, to aid layer detection. Slices were then mounted on slides using Fluoromount-G and allowed to dry overnight at room temperature. Images of the slices were obtained the following day using confocal microscope Leica SP5 with 20x dry objective, and each image showed AD/AV and claustrum projections, as well as NeuroTrace-labeled cell bodies, in separate channels.

Quantification and Statistical Analysis

Neuronal analysis and statistics

Multiple intrinsic neuronal properties were calculated as previously reported (Brennan et al., 2020). Briefly, spike threshold, spike amplitude, spike width, spike frequency adaptation ratio, latency to first spike, rheobase, input resistance (R_{in}), input capacitance (C_{in}), and membrane time constant (τ_m) were measured. Spike amplitude, threshold, and width were calculated from the average of all spikes in a 600 ms current step that elicited a 5 Hz spike train. Amplitude was calculated as the voltage difference from threshold to the peak of the spike, threshold from the peak of the third derivative of membrane potential (Cruikshank et al., 2012), and width as the full width at half-maximum spike amplitude. Spike frequency adaptation ratio was calculated from the same 600 ms current step protocol using the first sweep that elicited a 10 Hz spike train using the equation ISI_{last}/ISI_{first}. Latency to first spike and rheobase were measured

using a 1 sec current step protocol that began below threshold and increased by 1-5 pA steps until at least 3 sweeps post-threshold. Latency to first spike was calculated as the time from the onset of the current step to the peak of the first spike. Rheobase was measured as the minimum current needed to cause at least one spike in the 1 sec current step. Lastly, input resistance (R_{in}), input capacitance (C_{in}), and membrane time constant (τ_m) were all measured from a protocol that delivered a series of small negative current steps resulting in ~4 mV deflection in membrane potential. R_{in} was calculated using Ohm's law, mean voltage change divided by mean current. τ_m was measured by fitting a single exponential to the average of the initial 60 ms of the negative voltage deflection, ignoring the first 20 ms. Lastly, C_{in} was calculated using the formula $\tau_m = R_{in} \times C_{in}$. Statistical significance of the differences in intrinsic properties between the retrosplenial neuronal subtypes was calculated using the Wilcoxon rank sum test.

ChR2-assisted circuit mapping analysis and statistics

To quantify the effect of TC and ClaC input across the layers, the amplitude of the resulting postsynaptic responses from each laminar location of LED stimulation (L1a, L1/2, and cell body) were measured with a custom MATLAB script and/or Clampfit. The average of the response to the first pulse in the 10 Hz train was calculated for each cell at each LED laminar location. Significant differences between cell types and/or laminar locations were calculated using the Wilcoxon rank sum test. From the current step protocol, raster plots and PSTHs were plotted for each cell in MATLAB. The percent increase in spike rate was calculated by subtracting the number of spikes in a 100 ms window after the LED pulse from the number of spikes in a 100 ms window before the LED pulse, then dividing this value by the number of spikes in the 100 ms window before the LED pulse (Spikes Post – Spikes Pre / Spikes Pre). Significant differences between spike count pre- and post-stimulation for both LR and RS cells and LR and RS percent increase in spike rates were calculated using the Wilcoxon rank sum test.

Short-term dynamics were calculated from the 10 Hz LED pulses protocol (see Channelrhodopsin-assisted circuit mapping subsection of the Experimental Procedures section of Methods). Average response amplitudes of each pulse were measured for each cell. Amplitudes were then normalized using the equation stimulus n / stimulus 1, and normalized postsynaptic ratios were plotted. Cells with first pulse responses greater than 0.5 mV but not spiking were included. Significant differences between ratios of LR and RS neurons for each pulse were calculated using the Wilcoxon rank sum test.

Morphological analysis and statistics

Widths of RSG layers 1, 2, and 3 were measured in pixels and their boundaries delineated based on NeuroTrace expression using images in GIMP software. Layer 1 was distinguished by a low cell density, layer 2 by a thin, densely packed band of small pyramidal cell bodies, layer 3 by the lower density of small pyramidal neurons, and layer

5 as having larger cell bodies relative to layer 3. Representative image of RSG layers was selected as layer template for the analysis. Equivalent portions of the image were also taken from the AD/AV and claustrum image channels. Reconstructed cells were placed on the layer template to best represent their original position placement within the slice. After all images (both cell reconstructions and sample projections into RSG) were adjusted, they were turned into binary black and white images using ImageJ. Signal threshold (set as white pixels) was manually adjusted for each image using the Image -> Adjust -> Threshold option to best represent the data in the image.

Dendrites and TC/ClaC axons and terminal arbors were analyzed as a function of cortical depth (Yamawaki 2014 REF). Using custom Python scripts, white pixels in every image (axonal expression or reconstructed cell) were then counted, and their total counts per row were divided by the total numbers of white pixels in the image, resulting in a projection distribution vector along the layers of RSG. Density plots were visualized from distribution vectors in Python (with pandas, matplotlib, scipy, and Seaborn) and MATLAB software. Correlation matrix was created using pandas and scipy correlation with Pearson's method and plotted as a Seaborn heatmap. R-values were displayed on the map, while p-values were represented as the following symbols: * for $0.01 < p < 0.05$, ** for $0.001 < p < 0.01$, and *** for $p < 0.001$. Data was plotted as mean ± SEM. Images of axonal projection patterns to prefrontal cortex (PFC) and from contralateral RSG to RSG (Figure S6&S7) were obtained from the Allen Mouse Brain Connectivity Atlas (https://connectivity.brain-map.org; Oh et al., 2014).

Modeling methodology

Thalamocortical synapses from the matrix thalamic nuclei generally display facilitating short term dynamics. In contrast, synaptic input from anteroventral thalamus onto the apical dendrites of LR cells in RSG is depressing. Short term depression can act as a lowpass filter of presynaptic information (Lavian and Korngreen, 2019), but this function seems unlikely in the context of LR cells, which appear particularly well-suited to receiving high-frequency input. It is also known that subicular synapses onto LR cells are facilitating, suggesting they provide 'context' depolarization with which thalamic input onto apical dendrites interacts. To investigate the function of depressing synapses onto LR cells in this specific context, we studied the interaction of a biophysically realistic model of an LR cell (Brennan et al., 2020) with simulated short-term synaptic dynamics.

We implemented our biophysical LR model using NEURON (Carnevale and Hines, 2006). This model utilizes a Hodgkin-Huxley formalism, incorporating a fast sodium current, a delayed rectifier potassium current, an adaptation current, and a simulated Kv1 current capturing the observed late-spiking behavior of LR cells; equations and parameter specifications are previously reported (Brennan et al., 2020). To simulate short-term synaptic plasticity, we utilized the phenomenological model of Tsodyks-

Markram (Tsodyks et al., 1998). In this model, the proportion of synaptic resources available for release at time *t* is given by *x(t),* and the proportion of available resources that are released (i.e. the release probability) is given by *u(t)*. These quantities satisfy the equations

$$\frac{du}{dt} = -\frac{u}{\tau_f} + U(1 - u(t^-))\,\delta(t - t_{sp})$$

and

$$\frac{dx}{dt} = \frac{1 - x}{\tau_d} - u(t^+)x(t^-)\,\delta(t - t_{sp})$$

where τ_f and τ_d denote the time constants for *u*-decay and *x*-recovery, t_{sp} denotes any presynaptic spike time, and *U* is a parameter governing the magnitude of instantaneous resource release upon arrival of a presynaptic spike. We have used the notation $f(t^-)$ and $f(t^+)$ to respectively denote the right- and left-limits of *f* at *t*. In turn, these dynamics of *x* and *u* determine the post-synaptic current *I(t)*, given by the equation

$$\frac{dI}{dt} = -\frac{I}{\tau_s} + Au(t^+)x(t^-)\,\delta(t - t_{sp})$$

where τ_s denotes the time constant for *I*-decay, and *A* is a parameter governing the amplitude of post-synaptic current response to a presynaptic spike.

We generated Poisson spike trains and fed these to the Tsodyks-Markram model tuned with the parameter sets (Tsodyks and Wu, 2013):

STD: [τ_f, τ_d, τ_s, *U, A*] = [50 ms, 750 ms, 20 ms, 0.45, 1]
STF: [τ_f, τ_d, τ_s, *U, A*] = [750 ms, 50 ms, 20 ms, 0.15, 1]

which generate strong depressing and strong facilitating dynamics, respectively. For reference, when fed a 15 Hz evenly spaced spike train, the STD model produces an EPSC2/1 ratio of 0.66 and an EPSC6/1 ratio of 0.2. When fed the same 15 Hz evenly spaced spike train, the STF model produces an EPSC2/1 ratio of 1.7 and an EPSC6/1 ratio of 3.0. We post-processed the current waveform for each spike train by normalizing the currents to fix the average EPSC amplitude observed in each waveform. This has the effect of ensuring each current waveform conveys approximately the same total amount of charge, regardless of synaptic plasticity type (see supplement for numerical evidence). The normalized current waveforms were presented to the LR cell at an apical dendrite, along with a background current of $I_{crit} \approx$ 0.03625 nA presented at the soma, where I_{crit} is the value of step current at which the LR cell transitions from no activity to tonic firing at a nonzero frequency. This

background current was intended to simulate the depolarization provided by subicular "context input" to the basal dendrites.

The Poisson input spike trains were presented to the LR cell at one of two activity intervals, [10,60] ms or [200, 250] ms, roughly representing conditions under which the Kv1 late-spiking current is strong and weak, respectively (Figure 4B). We performed simulations under the two activity interval conditions, varying input spike frequency over a wide range from 10 Hz to 200 Hz, and varying synaptic plasticity type using the two parameter sets described above, with an average EPSC amplitude of 0.005 (0.003 nA and 0.007 nA obtained analogous results; data not shown). For each set of fixed synaptic plasticity parameters, EPSC amplitude, activity interval, and input frequency, we performed 500 trials. The Kruskal-Wallis test was used to assess whether the distributions of observed spike counts and spike latencies were significantly different between the STD and STF conditions, both at each frequency and when frequencies were pooled together.

In order to assess the hypothesis that the observed spiking advantage of STF over STD synapses results from interaction with the Kv1 current, we systematically varied the value of the maximum Kv1 conductance from 0.035 to 0.085 (where the canonical value used in the above trials was 0.075). All other parameters fixed, the relationship between g_{max} and the rheobase of the resulting cell is linear. Using simulation data, we estimated this linear function as Rheobase(g_{max}) = 0.80169 * g_{max}-0.025764 and used this estimate to compute, for each value of g_{max}, the somatic background current required to place the LR model just below its spiking threshold (as in the previous trials). We then once again applied apical EPSCs of average strength 0.005 nA, over frequencies ranging from 50 to 250 Hz. For each combination of g_{max}, input frequency, and synaptic type, we performed 1500 trials under the early spike window condition and 1200 trials under the late spike window condition. To quantify the size of the STF/STD advantage, we calculated, for each value of g_{max}, the difference between the mean spike count for STF trials and the mean spike count for STD trials (in both cases, averaged over all frequencies >100 Hz). To quantify the presence of any relationship between g_{max} and the mean spike difference, we computed the Pearson correlation coefficient between these two variables and performed a two-sided Wald test to assess the null hypothesis that the correlation coefficient equals zero.

REFERENCES

Alexander AS, Carstensen LC, Hinman JR, Raudies F, William Chapman G, Hasselmo ME. 2020. Egocentric boundary vector tuning of the retrosplenial cortex. *Sci Adv* **6**:eaaz2322. doi:10.1126/sciadv.aaz2322

Alexander AS, Nitz DA. 2017. Spatially Periodic Activation Patterns of Retrosplenial Cortex Encode Route Sub-spaces and Distance Traveled. doi:10.1016/j.cub.2017.04.036

Alexander AS, Rangel LM, Tingley D, Nitz DA. 2018. Neurophysiological signatures of temporal coordination between retrosplenial cortex and the hippocampal formation. *Behav Neurosci* **132**:453–468. doi:10.1037/bne0000254

Alfano C, Studer M. 2013. Neocortical arealization: Evolution, mechanisms, and open questions. *Dev Neurobiol* **73**:411–447. doi:10.1002/dneu.22067

Anastasiades PG, Collins DP, Carter AG. 2020. Mediodorsal and ventromedial thalamus engage distinct L1 circuits in the prefrontal cortex. *bioRxiv*. doi:10.1101/2020.01.08.898817

Bicanski A, Burgess N. 2020. Neuronal vector coding in spatial cognition. *Nat Rev Neurosci*. doi:10.1038/s41583-020-0336-9

Brennan EKW, Sudhakar SK, Jedrasiak-Cape I, John TT, Ahmed OJ. 2020. Hyperexcitable Neurons Enable Precise and Persistent Information Encoding in the Superficial Retrosplenial Cortex. *CellReports* **30**:1598-1612.e8. doi:10.1016/j.celrep.2019.12.093

Brown SP, Mathur BN, Olsen SR, Luppi PH, Bickford ME, Citri A. 2017. New breakthroughs in understanding the role of functional interactions between the neocortex and the claustrum. *J Neurosci* **37**:10877–10881. doi:10.1523/JNEUROSCI.1837-17.2017

Burgess N, Becker S, King JA, O'Keefe J. 2001. Memory for events and their spatial context: Models and experimentsPhilosophical Transactions of the Royal Society B: Biological Sciences. Royal Society. pp. 1493–1503. doi:10.1098/rstb.2001.0948

Burman KJ, Reser DH, Richardson KE, Gaulke H, Worthy KH, Rosa MGP. 2011. Subcortical projections to the frontal pole in the marmoset monkey. *Eur J Neurosci* **34**:303–319. doi:10.1111/j.1460-9568.2011.07744.x

Byrne P, Becker S, Burgess N. 2007. Remembering the past and imagining the future: A neural model of spatial memory and imagery. *Psychol Rev* **114**:340–375. doi:10.1037/0033-295X.114.2.340

Carnevale NT, Hines ML. 2006. The NEURON Book. Cambridge: Cambridge University Press.

Cho J-H, Rendall SD, Gray JM. 2017. Brain-wide maps of Fos expression during fear learning and recall. *Learn Mem* **24**:169–181. doi:10.1101/lm.044446

Chrastil ER. 2018. Heterogeneity in human retrosplenial cortex: A review of function and connectivity. *Behav Neurosci*.

Clascá F, Rubio-Garrido P, Jabaudon D. 2012. Unveiling the diversity of thalamocortical neuron subtypes. *Eur J Neurosci* **35**:1524–1532. doi:10.1111/j.1460-9568.2012.08033.x

Collins DP, Anastasiades PG, Marlin JJ, Correspondence AGC. 2018. Reciprocal Circuits Linking the Prefrontal Cortex with Dorsal and Ventral Thalamic Nuclei.

Neuron **98**:366-379.e4. doi:10.1016/j.neuron.2018.03.024
Corcoran KA, Donnan MD, Tronson NC, Guzmán YF, Gao C, Jovasevic V, Guedea AL, Radulovic J. 2011. NMDA receptors in retrosplenial cortex are necessary for retrieval of recent and remote context fear memory. *J Neurosci* **31**:11655–11659. doi:10.1523/JNEUROSCI.2107-11.2011
Corcoran KA, Frick BJ, Radulovic J, Kay LM. 2016. Analysis of coherent activity between retrosplenial cortex, hippocampus, thalamus, and anterior cingulate cortex during retrieval of recent and remote context fear memory. *Neurobiol Learn Mem* **127**:93–101. doi:10.1016/j.nlm.2015.11.019
Crick FC, Koch C. 2005. What is the function of the claustrum? *Philos Trans R Soc B Biol Sci* **360**:1271–1279. doi:10.1098/rstb.2005.1661
Cruikshank SJ, Ahmed OJ, Stevens TR, Patrick SL, Gonzalez AN, Elmaleh M, Connors BW. 2012. Thalamic control of layer 1 circuits in prefrontal cortex. *J Neurosci* **32**:17813–17823.
Da Costa NM, Fürsinger D, Martin KAC. 2010. The synaptic organization of the claustral projection to the cat's visual cortex. *J Neurosci* **30**:13166–13170. doi:10.1523/JNEUROSCI.3122-10.2010
Delevich K, Tucciarone J, Huang ZJ, Li B. 2015. The mediodorsal thalamus drives feedforward inhibition in the anterior cingulate cortex via parvalbumin interneurons. *J Neurosci* **35**:5743–5753. doi:10.1523/JNEUROSCI.4565-14.2015
Derdikman D. 2009. Are the boundary-related cells in the subiculum boundary-vector cells? *J Neurosci*. doi:10.1523/JNEUROSCI.4176-09.2009
Epstein RA. 2008. Parahippocampal and retrosplenial contributions to human spatial navigation. *Trends Cogn Sci* **12**:388–396.
Feldmeyer D, Brecht M, Helmchen F, Petersen CCH, Poulet JFA, Staiger JF, Luhmann HJ, Schwarz C. 2013. Barrel cortex function. *Prog Neurobiol*. doi:10.1016/j.pneurobio.2012.11.002
Galloni AR, Laffere A, Rancz E. 2020. Apical length governs computational diversity of layer 5 pyramidal neurons. *Elife* **9**. doi:10.7554/eLife.55761
Geijo-barrientos E, Martínez S, Sempere-ferràndez A. 2019. Synaptic mechanisms underlying the intense firing of neocortical layer 5B pyramidal neurons in response to cortico-cortical inputs. *Brain Struct Funct* 1–14. doi:10.1007/s00429-019-01842-8
Goll Y, Atlan G, Citri A. 2015. Attention: The claustrum. *Trends Neurosci*. doi:10.1016/j.tins.2015.05.006
Guo K, Yamawaki N, Svoboda K, Shepherd GMG. 2018. Anterolateral motor cortex connects with a medial subdivision of ventromedial thalamus through cell type-specific circuits, forming an excitatory thalamo-cortico-thalamic loop via layer 1 apical tuft dendrites of layer 5B pyramidal tract type neurons. *J Neurosci* **38**:8787–8797. doi:10.1523/JNEUROSCI.1333-18.2018
Han CJ, O'Tuathaigh CM, Van Trigt L, Quinn JJ, Fanselow MS, Mongeau R, Koch C, Anderson DJ. 2003. Trace but not delay fear conditioning requires attention and the anterior cingulate cortex. *Proc Natl Acad Sci U S A* **100**:13087–13092. doi:10.1073/pnas.2132313100
Hanbery J, Jasper H. 1953. Independence of diffuse thalamo-cortical projection system shown by specific nuclear destructions. *J Neurophysiol* **16**:252–271.
Herkenham M. 1986. New Perspectives on the Organization and Evolution of

Nonspecific Thalamocortical Projections. Springer, Boston, MA. pp. 403–445. doi:10.1007/978-1-4613-2149-1_11
Herkenham M. 1980. Laminar Organization of Thalamic Projections to Rat Neocortex. *Science (80-)* **179**:283–285. doi:10.1126/science.179.4070.283
Hestrin S, Armstrong WE. 1996. Morphology and physiology of cortical neurons in layer I. *J Neurosci* **16**:5290–5300. doi:10.1523/jneurosci.16-17-05290.1996
Hinman JR, Dannenberg H, Alexander AS, Hasselmo ME. 2018. Neural mechanisms of navigation involving interactions of cortical and subcortical structures. *J Neurophysiol*. doi:10.1152/jn.00498.2017
Holmgren C, Harkany T, Svennenfors B, Zilberter Y. 2003. Pyramidal cell communication within local networks in layer 2/3 of rat neocortex. *J Physiol* **551**:139–153. doi:10.1111/j.1469-7793.2003.00139.x
Ichinohe N, Knight A, Ogawa M, Ohshima T, Mikoshiba K, Yoshihara Y, Terashima T, Rockland KS. 2008. Unusual patch-matrix organization in the retrosplenial cortex of the reeler mouse and shaking rat kawasaki. *Cereb Cortex* **18**:1125–1138. doi:10.1093/cercor/bhm148
Ichinohe N, Yoshihara Y, Hashikawa T, Rockland KS. 2003. Developmental study of dendritic bundles in layer 1 of the rat granular retrosplenial cortex with special reference to a cell adhesion molecule, OCAM. *Eur J Neurosci* **18**:1764–1774. doi:10.1046/j.1460-9568.2003.02900.x
Ipser JC, Singh L, Stein DJ. 2013. Meta-analysis of functional brain imaging in specific phobia. *Psychiatry Clin Neurosci* **67**:311–322. doi:10.1111/pcn.12055
Jackson J, Karnani MM, Zemelman B V, Burdakov D, Lee AK. 2018. Inhibitory Control of Prefrontal Cortex by the Claustrum. *Neuron* **99**:1029-1039.e4. doi:10.1016/j.neuron.2018.07.031
Jiang X, Shen S, Cadwell CR, Berens P, Sinz F, Ecker AS, Patel S, Tolias AS. 2015. Principles of connectivity among morphologically defined cell types in adult neocortex. *Science (80-)* **350**. doi:10.1126/science.aac9462
Jones EG. 2001. The thalamic matrix and thalamocortical synchrony. *Trends Neurosci*. doi:10.1016/S0166-2236(00)01922-6
Jones EG. 1998. Viewpoint: The core and matrix of thalamic organization. *Neuroscience*. doi:10.1016/S0306-4522(97)00581-2
Kawaguchi Y, Kubota Y. 1997. GABAergic cell subtypes and their synaptic connections in rat frontal cortex. *Cereb Cortex* **7**:476–486.
Keene CS, Bucci DJ. 2008a. Contributions of the Retrosplenial and Posterior Parietal Cortices to Cue-Specific and Contextual Fear Conditioning. *Behav Neurosci* **122**:89–97. doi:10.1037/0735-7044.122.1.89
Keene CS, Bucci DJ. 2008b. Neurotoxic Lesions of Retrosplenial Cortex Disrupt Signaled and Unsignaled Contextual Fear Conditioning. *Behav Neurosci* **122**:1070–1077. doi:10.1037/a0012895
Kim EJ, Juavinett AL, Kyubwa EM, Jacobs MW, Callaway EM. 2015. Three Types of Cortical Layer 5 Neurons That Differ in Brain-wide Connectivity and Function. *Neuron* **88**:1253–1267. doi:10.1016/j.neuron.2015.11.002
Kim J, Matney CJ, Roth RH, Brown SP. 2016. Synaptic organization of the neuronal circuits of the claustrum. *J Neurosci* **36**:773–784. doi:10.1523/JNEUROSCI.3643-15.2016

Kitanishi T, Matsuo N. 2017. Organization of the claustrum-to-entorhinal cortical connection in mice. *J Neurosci* **37**:269–280. doi:10.1523/JNEUROSCI.1360-16.2016

Kurotani T, Miyashita T, Wintzer M, Konishi T, Sakai K, Ichinohe N, Rockland KS. 2013. Pyramidal neurons in the superficial layers of rat retrosplenial cortex exhibit a late-spiking firing property. *Brain Struct Funct* **218**:239–254. doi:10.1007/s00429-012-0398-1

Kwapis JL, Jarome TJ, Lee JL, Gilmartin MR, Helmstetter FJ. 2014. Extinguishing trace fear engages the retrosplenial cortex rather than the amygdala. *Neurobiol Learn Mem* **113**:41–54. doi:10.1016/j.nlm.2013.09.007

Kwapis JL, Jarome TJ, Lee JL, Helmstetter FJ. 2015. The retrosplenial cortex is involved in the formation of memory for context and trace fear conditioning. *Neurobiol Learn Mem* **123**:110–116. doi:10.1016/j.nlm.2015.06.007

Lavian H, Korngreen A. 2019. Short-term depression shapes information transmission in a constitutively active GABAergic synapse. *Sci Rep* **9**:1–15. doi:10.1038/s41598-019-54607-y

Lever C, Burton S, Jeewajee A, O'Keefe J, Burgess N. 2009. Boundary vector cells in the subiculum of the hippocampal formation. *J Neurosci* **29**:9771–9777. doi:10.1523/JNEUROSCI.1319-09.2009

Lorento de No R. 1938. Cerebral cortex: Architecture, intracortical connections, motor projectionsPhysiology of the Nervous System. pp. 291–340.

Maguire E. 2001. The retrosplenial contribution to human navigation: a review of lesion and neuroimaging findings. *Scand J Psychol* **42**:225–238.

Majak K, Pikkarainen M, Kemppainen S, Jolkkonen E, Pitkänen A. 2002. Projections from the amygdaloid complex to the claustrum and the endopiriform nucleus: A *Phaseolus vulgaris* leucoagglutinin study in the rat. *J Comp Neurol* **451**:236–249. doi:10.1002/cne.10346

Morison RS, Dempsey EW. 1941. A STUDY OF THALAMO-CORTICAL RELATIONS. *Am J Physiol Content* **135**:281–292. doi:10.1152/ajplegacy.1941.135.2.281

Narikiyo K, Mizuguchi R, Ajima A, Shiozaki M, Hamanaka H, Johansen JP, Mori K, Yoshihara Y. 2020. The claustrum coordinates cortical slow-wave activity. *Nat Neurosci* **23**:741–753. doi:10.1038/s41593-020-0625-7

Nitzan N, McKenzie S, Beed P, English DF, Oldani S, Tukker JJ, Buzsáki G, Schmitz D. 2020. Propagation of hippocampal ripples to the neocortex by way of a subiculum-retrosplenial pathway. *Nat Commun* **11**:1–17. doi:10.1038/s41467-020-15787-8

O'Mara S. 2013. The anterior thalamus provides a subcortical circuit supporting memory and spatial navigation. *Front Syst Neurosci* **7**. doi:10.3389/fnsys.2013.00045

Odagiri S, Meguro R, Asano Y, Tani T, Ichinohe N. 2011. Single Axon Branching Analysis in Rat Thalamocortical Projection from the Anteroventral Thalamus to the Granular Retrosplenial Cortex. *Front Neuroanat* **5**:63. doi:10.3389/fnana.2011.00063

Oh SW, Harris JA, Ng L, Winslow B, Cain N, Mihalas S, Wang Q, Lau C, Kuan L, Henry AM, Mortrud MT, Ouellette B, Nguyen TN, Sorensen SA, Slaughterbeck CR, Wakeman W, Li Y, Feng D, Ho A, Nicholas E, Hirokawa KE, Bohn P, Joines KM, Peng H, Hawrylycz MJ, Phillips JW, Hohmann JG, Wohnoutka P, Gerfen CR, Koch C, Bernard A, Dang C, Jones AR, Zeng H. 2014. A mesoscale connectome of the

mouse brain. *Nature* **508**:207–214. doi:10.1038/nature13186
Olson JM, Tongprasearth K, Nitz DA. 2017. Subiculum neurons map the current axis of travel. *Nat Neurosci* **20**:170–172. doi:10.1038/nn.4464
Overstreet-Wadiche L, McBain CJ. 2015. Neurogliaform cells in cortical circuits. *Nat Rev Neurosci*. doi:10.1038/nrn3969
Peters A. 1979. Thalamic input to the cerebral cortex. *Trends Neurosci* **2**:183–185. doi:10.1016/0166-2236(79)90074-2
Peters A, Feldman ML. 1976. The projection of the lateral geniculate nucleus to area 17 of the rat cerebral cortex. I. General description. *J Neurocytol* **5**:63–84. doi:10.1007/BF01176183
Peyrache A, Lacroix MM, Petersen PC, Buzsáki G. 2015. Internally organized mechanisms of the head direction sense. *Nat Neurosci* **18**:569–575. doi:10.1038/nn.3968
Renouard L, Billwiller F, Ogawa K, Clément O, Camargo N, Abdelkarim M, Gay N, Scoté-Blachon C, Touré R, Libourel PA, Ravassard P, Salvert D, Peyron C, Claustrat B, Léger L, Salin P, Malleret G, Fort P, Luppi PH. 2015. The supramammillary nucleus and the claustrum activate the cortex during REM sleep. *Sci Adv* **1**:e1400177. doi:10.1126/sciadv.1400177
Rodriguez-Moreno J, Porrero C, Rollenhagen A, Rubio-Teves M, Casas-Torremocha D, Alonso-Nanclares L, Yakoubi R, Santuy A, Merchan-Pérez A, DeFelipe J, Lübke JHR, Clasca F. 2020. Area-specific synapse structure in branched posterior nucleus axons reveals a new level of complexity in thalamocortical networks. *J Neurosci* **40**:2663–2679. doi:10.1523/JNEUROSCI.2886-19.2020
Rubio-Garrido P, Pe´rezpe´rez-De-Manzo F, Porrero CC, Galazo MJ, Clasca´1 FC. 2009. Thalamic Input to Distal Apical Dendrites in Neocortical Layer 1 Is Massive and Highly Convergent. *Cereb Cortex Oct* **19**:2380–2395. doi:10.1093/cercor/bhn259
Salerno MT, Cortimiglia R, Crescimanno G, Amato G, Infantellina F. 1984. Effects of claustrum stimulation on spontaneous bioelectrical activity of motor cortex neurons in the cat. *Exp Neurol* **86**:227–239. doi:10.1016/0014-4886(84)90183-3
Sempere-Ferràndez A, Andrés-Bayón B, Geijo-Barrientos E. 2018. Callosal responses in a retrosplenial column. *Brain Struct Funct* **223**:1051–1069. doi:10.1007/s00429-017-1529-5
Shibata H. 1993. Efferent projections from the anterior thalamic nuclei to the cingulate cortex in the rat. *J Comp Neurol* **330**:533–542. doi:10.1002/cne.903300409
Sigwald EL, de Olmos S, Lorenzo A. 2020. Retrograde and anterograde contextual fear amnesia induced by selective elimination of layer IV-Va neurons in the granular retrosplenial cortex (A29). *Neurobiol Learn Mem* **171**:107229. doi:10.1016/j.nlm.2020.107229
Simonnet J, Brecht M. 2019. Burst firing and spatial coding in subicular principal cells. *J Neurosci* **39**:3651–3662. doi:10.1523/JNEUROSCI.1656-18.2019
Smith JB, Radhakrishnan H, Alloway KD. 2012. Rat claustrum coordinates but does not integrate somatosensory and motor cortical information. *J Neurosci* **32**:8583–8588. doi:10.1523/JNEUROSCI.1524-12.2012
Smythies J, Edelstein L, Ramachandran V. 2012. Hypotheses relating to the function of the claustrum. *Front Integr Neurosci* **6**. doi:10.3389/fnint.2012.00053

Spiers HJ, Barry C. 2015. Neural systems supporting navigation. *Curr Opin Behav Sci*. doi:10.1016/j.cobeha.2014.08.005
Sripanidkulchai K, Wyss JM. 1987. The laminar organization of efferent neuronal cell bodies in the retrosplenial granular cortex. *Brain Res* **406**:255–269. doi:10.1016/0006-8993(87)90790-6
Steenland HW, Li X-Y, Zhuo M. 2012. Predicting Aversive Events and Terminating Fear in the Mouse Anterior Cingulate Cortex during Trace Fear Conditioning. doi:10.1523/JNEUROSCI.5566-11.2012
Stewart S, Jeewajee A, Wills TJ, Burgess N, Lever C. 2014. Boundary coding in the rat subiculum. *Philos Trans R Soc B Biol Sci* **369**:20120514. doi:10.1098/rstb.2012.0514
Todd TP, Bucci DJ. 2015. Retrosplenial Cortex and Long-Term Memory: Molecules to Behavior. *Neural Plast* **2015**:9. doi:10.1155/2015/414173
Todd TP, DeAngeli NE, Jiang MY, Bucci DJ. 2017. Retrograde amnesia of contextual fear conditioning: Evidence for retrosplenial cortex involvement in configural processing. *Behav Neurosci* **131**:46–54. doi:10.1037/bne0000183
Tsanov M, Chah E, Vann SD, Reilly RB, Erichsen JT, Aggleton JP, O'Mara SM. 2011. Theta-modulated head direction cells in the rat anterior thalamus. *J Neurosci* **31**:9489–9502. doi:10.1523/JNEUROSCI.0353-11.2011
Tsodyks M, Pawelzik K, Markram H. 1998. Neural Networks with Dynamic Synapses. *Neural Comput* **10**:821–835. doi:10.1162/089976698300017502
Tsodyks M, Wu S. 2013. Short-term synaptic plasticity. *Scholarpedia* **8**:3153. doi:10.4249/scholarpedia.3153
Vakolyuk NI, Kosterina A V, Shlumukova AR. 1980. Spontaneous Electrical Activity of the Claustrum. *Neurophysiology* **12**:113–120.
Valenstein E, Bowers D, Verfaellie M, Heilman KM, Day A, Watson RT. 1987. Retrosplenial amnesia. *Brain* **110**:1631–1646.
Van Der Werf YD, Witter MP, Groenewegen HJ. 2002. T he intralaminar and midline nuclei of the thalamus. Anatomical and functional evidence for participation in processes of arousal and awareness, Brain Research Reviews.
van Groen T, Wyss JM. 2003. Connections of the retrosplenial granular b cortex in the rat. *J Comp Neurol* **463**:249–263. doi:10.1002/cne.10757
van Groen T, Wyss JM. 1995. Projections from the anterodorsal and anteroveniral nucleus of the thalamus to the limbic cortex in the rat. *J Comp Neurol* **358**:584–604. doi:10.1002/cne.903580411
van Groen T, Wyss JM. 1990. Connections of the retrosplenial granular a cortex in the rat. *J Comp Neurol* **300**:593–606. doi:10.1002/cne.903000412
Vann SD, Aggleton JP, Maguire EA. 2009. What does the retrosplenial cortex do? *Nat Rev Neurosci* **10**:792–802. doi:10.1038/nrn2733
Vetere G, Kenney JW, Tran LM, Xia F, Steadman PE, Parkinson J, Josselyn SA, Frankland PW. 2017. Chemogenetic Interrogation of a Brain-wide Fear Memory Network in Mice. *Neuron* **94**:363-374.e4. doi:10.1016/j.neuron.2017.03.037
Vetere G, Restivo L, Cole CJ, Ross PJ, Ammassari-Teule M, Josselyn SA, Frankland PW. 2011. Spine growth in the anterior cingulate cortex is necessary for the consolidation of contextual fear memory. *Proc Natl Acad Sci U S A* **108**:8456–8460. doi:10.1073/pnas.1016275108

Wang Q, Ng L, Harris JA, Feng D, Li Y, Royall JJ, Oh SW, Bernard A, Sunkin SM, Koch C, Zeng H. 2017. Organization of the connections between claustrum and cortex in the mouse. *J Comp Neurol* **525**:1317–1346. doi:10.1002/cne.24047

White MG, Mathur BN. 2018. Frontal cortical control of posterior sensory and association cortices through the claustrum. *Brain Struct Funct* **223**:2999–3006. doi:10.1007/s00429-018-1661-x

Wyss JM, van Groen T. 1992. Connections between the retrosplenial cortex and the hippocampal formation in the rat: A review. *Hippocampus* **2**:1–11. doi:10.1002/hipo.450020102

Wyss MJ, Van Groen T, Sripanidkulchai K. 1990. Dendritic bundling in layer I of granular retrosplenial cortex: Intracellular labeling and selectivity of innervation. *J Comp Neurol* **295**:33–42. doi:10.1002/cne.902950104

Yamawaki N, Borges K, Suter BA, Harris KD, Shepherd GMG. 2014. A genuine layer 4 in motor cortex with prototypical synaptic circuit connectivity. *Elife* **3**:e05422. doi:10.7554/eLife.05422

Yamawaki N, Corcoran KA, Guedea AL, Shepherd GMG, Radulovic J. 2019a. Differential Contributions of Glutamatergic Hippocampal→Retrosplenial Cortical Projections to the Formation and Persistence of Context Memories. *Cereb Cortex* **29**:2728–2736. doi:10.1093/cercor/bhy142

Yamawaki N, Li X, Lambot L, Ren LY, Radulovic J, Shepherd GM. 2019b. Long-range inhibitory intersection of a retrosplenial thalamocortical circuit by apical tuft-targeting CA1 neurons. *Nat Neurosci* 1. doi:10.1101/427179

Yamawaki N, Radulovic J, Shepherd GMG. 2016a. A corticocortical circuit directly links retrosplenial cortex to M2 in the mouse. *J Neurosci* **36**:9365–9374.

Yamawaki N, Suter BA, Wickersham IR, Shepherd GMG. 2016b. Combining optogenetics and electrophysiology to analyze projection neuron circuits. *Cold Spring Harb Protoc* **2016**:840–847. doi:10.1101/pdb.prot090084

Yousuf H, Nye AN, Moyer, Jr. JR. 2020. Heterogeneity of Neuronal Firing Type and Morphology in Retrosplenial Cortex of Male F344 Rats. *J Neurophysiol* **123**. doi:10.1152/jn.00577.2019

Zhao MG, Ko SW, Wu LJ, Toyoda H, Xu H, Quan J, Li J, Jia Y, Ren M, Xu ZC, Zhuo M. 2006. Enhanced presynaptic neurotransmitter release in the anterior cingulate cortex of mice with chronic pain. *J Neurosci* **26**:8923–8930. doi:10.1523/JNEUROSCI.2103-06.2006

Zingg B, Dong HW, Tao HW, Zhang LI. 2018. Input–output organization of the mouse claustrum. *J Comp Neurol* **526**:2428–2443. doi:10.1002/cne.24502

SUPPLEMENTAL INFORMATION

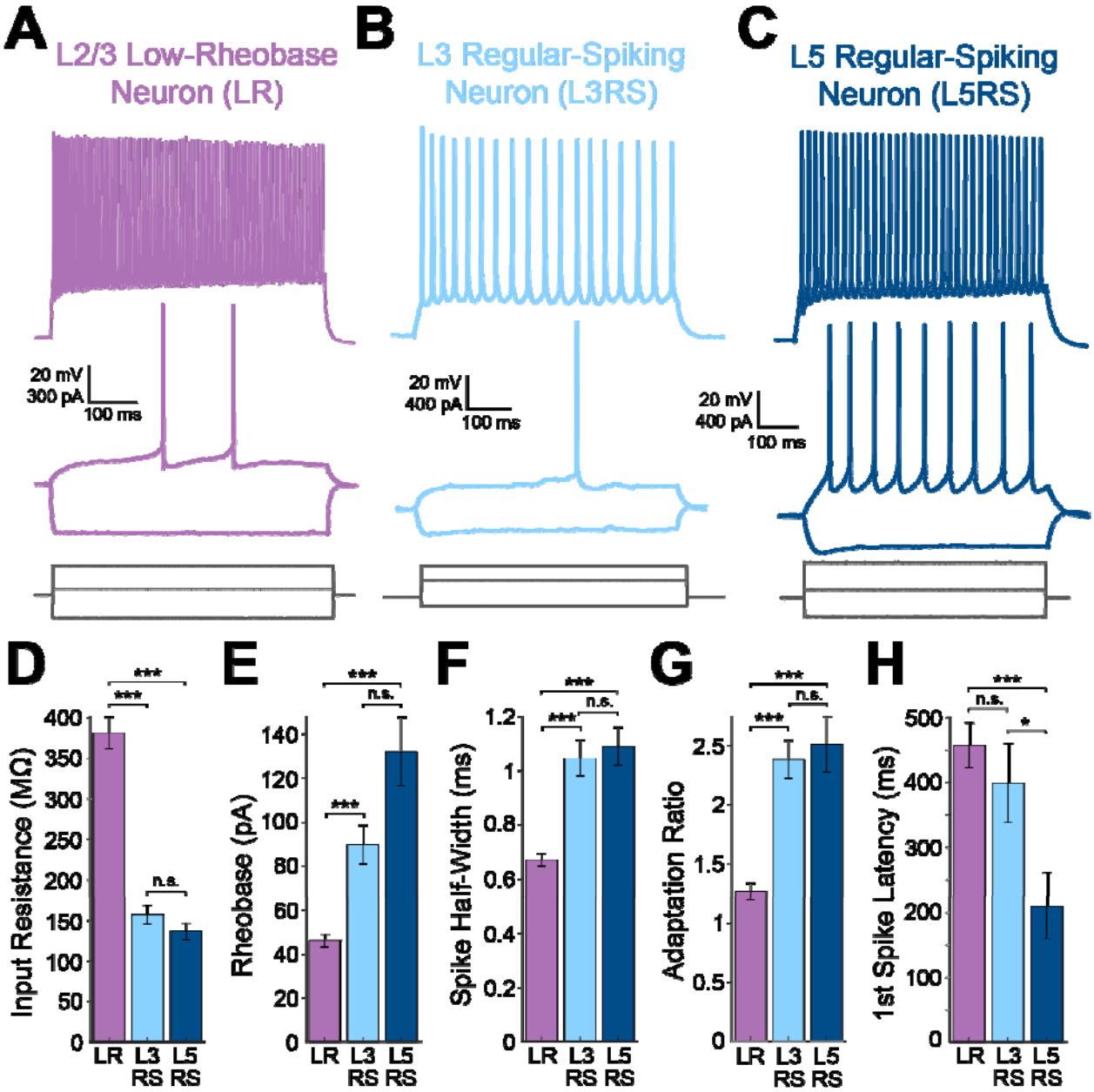

Figure S1. Intrinsic properties of RSG LR, layer 3 RS, and layer 5 RS neurons. (Related to Figures 1-6)

- ***A.*** Firing properties of a low-rheobase (LR) neuron in RSG layer 3. Top trace: Ability to fire sustained high-frequency spike trains. Middle trace: Near-threshold current injection results in a substantial delay to first spike. Bottom: injected current amplitudes for the voltage responses shown above.
- ***B.*** Same as ***A*** but for a layer 3 regular-spiking (L3 RS) neuron. Note the spike frequency adaptation at higher current injections and modest delay to first spike at near-threshold current injections.
- ***C.*** Same as ***A*** but for a layer 5 regular-spiking (L5 RS) neuron. Note the bursting phenotype at higher current injections and a relative lack of delay to first spike at near-threshold current injections.

D. Average input resistance (IR) for LR, L3 RS, and L5 RS neurons. Note the significantly larger IR in LR neurons compared to L3 RS ($p = 5.66e-12$; Wilcoxon rank sum test) and L5 RS cells ($p = 4.47e-13$; Wilcoxon rank sum test), while L3 and L5 RS cells do not differ ($p = 0.234$; Wilcoxon rank sum test).

E. Average rheobase for LR, L3 RS, and L5 RS neurons. Note the significantly lower rheobase in LR neurons compared to L3 RS ($p = 0.00019$; Wilcoxon rank sum test) and L5 RS cells ($p = 3.86e-09$; Wilcoxon rank sum test), while L3 and L5 RS cells do not differ ($p = 0.0673$; Wilcoxon rank sum test).

F. Average spike half-width for LR, L3 RS, and L5 RS neurons. Note the significantly narrower spike width in LR neurons compared to L3 RS (2.36e-07; Wilcoxon rank sum test) and L5 RS cells ($p = 6.40e-08$; Wilcoxon rank sum test), while L3 and L5 RS cells do not differ ($p = 0.6947$; Wilcoxon rank sum test).

G. Average spike adaptation ratio for LR, L3 RS, and L5 RS neurons. Note the significant lack of spike frequency adaptation in LR neurons compared to L3 RS ($p = 9.40e-11$; Wilcoxon rank sum test) and L5 RS cells ($p = 3.60e-10$; Wilcoxon rank sum test), while L3 and L5 RS cells do not differ ($p = 0.9058$; Wilcoxon rank sum test).

H. Average latency to first spike for LR, L3 RS, and L5 RS neurons. Note the lack of significant difference between layer 3 LR and RS neurons ($p = 0.3271$; Wilcoxon rank sum test). Layer 5 RS neurons have significantly shorter latency to first spike than both LR ($p = 0.0000539$; Wilcoxon rank sum test) and L3 RS neurons ($p = 0.0341$; Wilcoxon rank sum test). Error bars represent SEM in each panel.

.

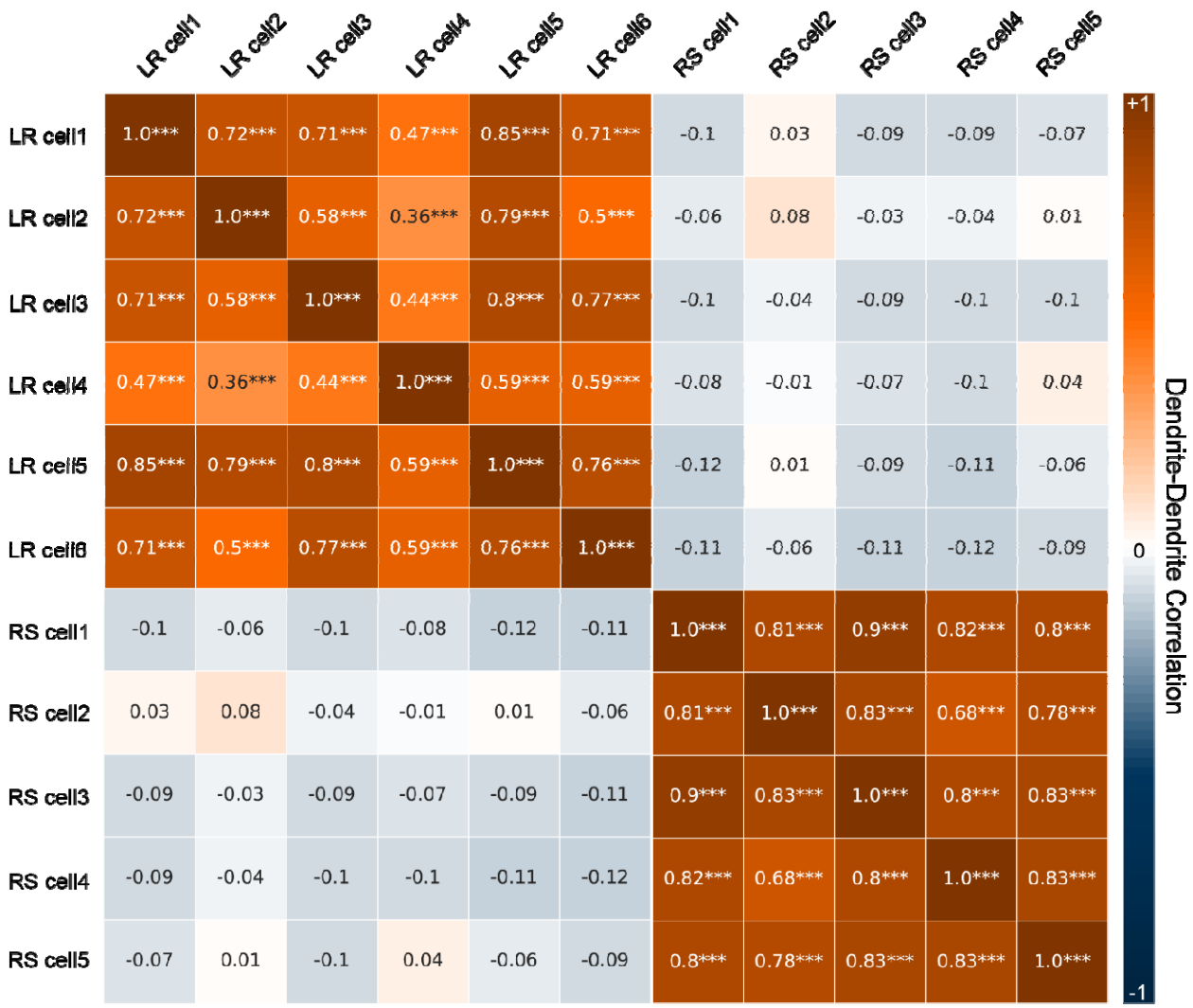

Figure S2. Dendrite-dendrite correlation map reveals consistent subtype-specific laminar dendritic structure. (Related to Figures 2&5). Dendritic arborizations across all reconstructed LR cells are positively correlated with each other but uncorrelated with layer 3 RS dendritic arborizations. Similarly, dendritic arborizations from all reconstructed layer 3 RS cells are positively correlated with each other but uncorrelated with LR dendritic arbors. Thus, dendritic morphology among LR and layer 3 RS cells is consistent. Numerical values in each box indicate R values, while p-values are represented as following: * for $0.01 < p < 0.05$, ** for $0.001 < p < 0.01$, *** for $p < 0.001$. Exact p-values are reported in Table S2.

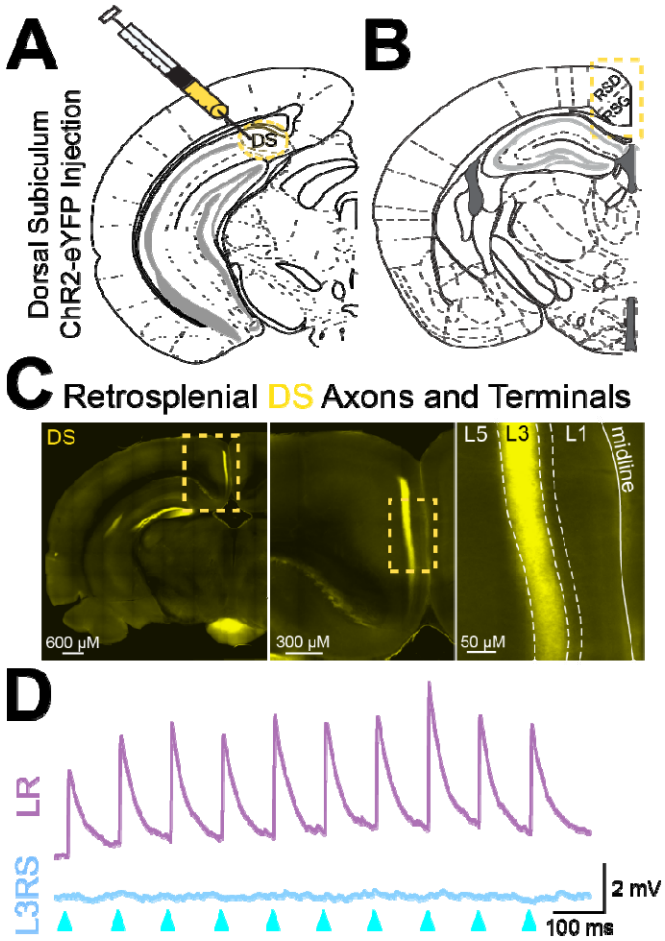

Figure S3. Dorsal subiculum axons and terminal arbors precisely target layer 3 of RSG and drive LR, but not RS, neurons. (Related to Discussion)

- ***A.*** Schematic showing injection of optogenetic viral construct AAV2-hsyn-ChR2-eYFP into dorsal subiculum (see Methods).
- ***B.*** Schematic showing target recording region in RSG.
- ***C.*** Left: Epiflourescent image of recorded retrosplenial slice showing fluorescing dorsal subiculum axons and terminal arbors in RSG. Middle: Zoom in on all of RSC from the box indicated in left panel. Right: Zoom in on superficial layers of RSG from the box indicated in middle panel. eYFP-expressing dorsal subiculum axons and terminal arbors are precisely localized to layer 3 of RSG.
- ***D.*** Trace examples from a same-slice sequential pair of LR (purple) and layer 3 RS (blue) neurons showing larger EPSPs in LR neurons compared to RS (which did not exhibit response) in response to a 10 Hz optogenetic pulse train. Blue triangles indicate each LED pulse. Cells were held at -65 mV.

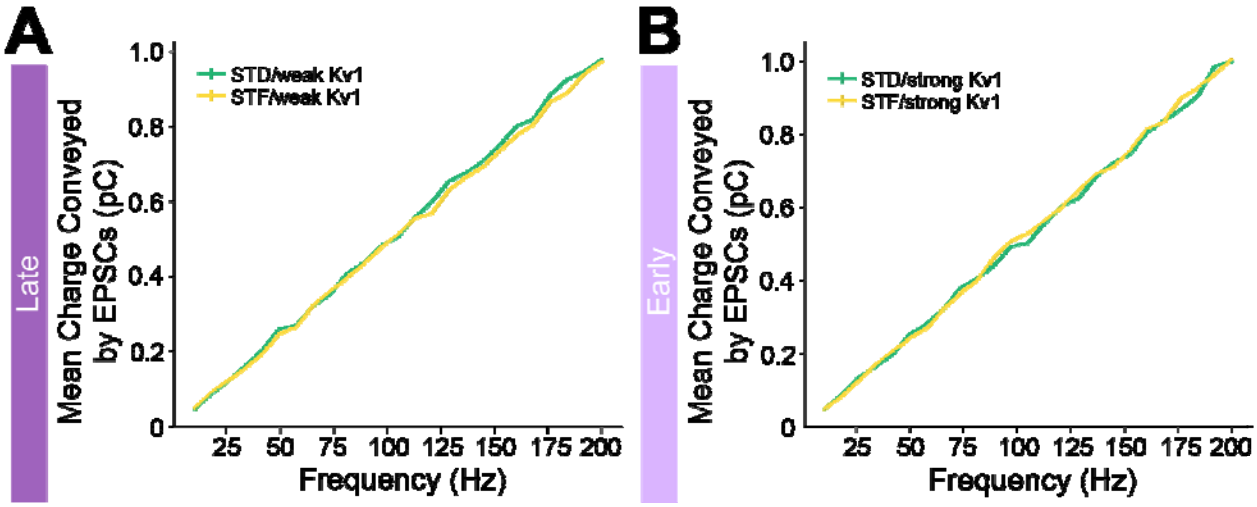

Figure S4. Total charge conveyed to the LR model in simulations is matched between the STD and STF conditions. (Related to Figure 4)

A. For each stimulation frequency, late spiking window trials in which the synapse displayed STD (green) and STF (yellow) dynamics conveyed the same quantity of charge, on average.

B. Same as ***A*** for early spiking widow trials.

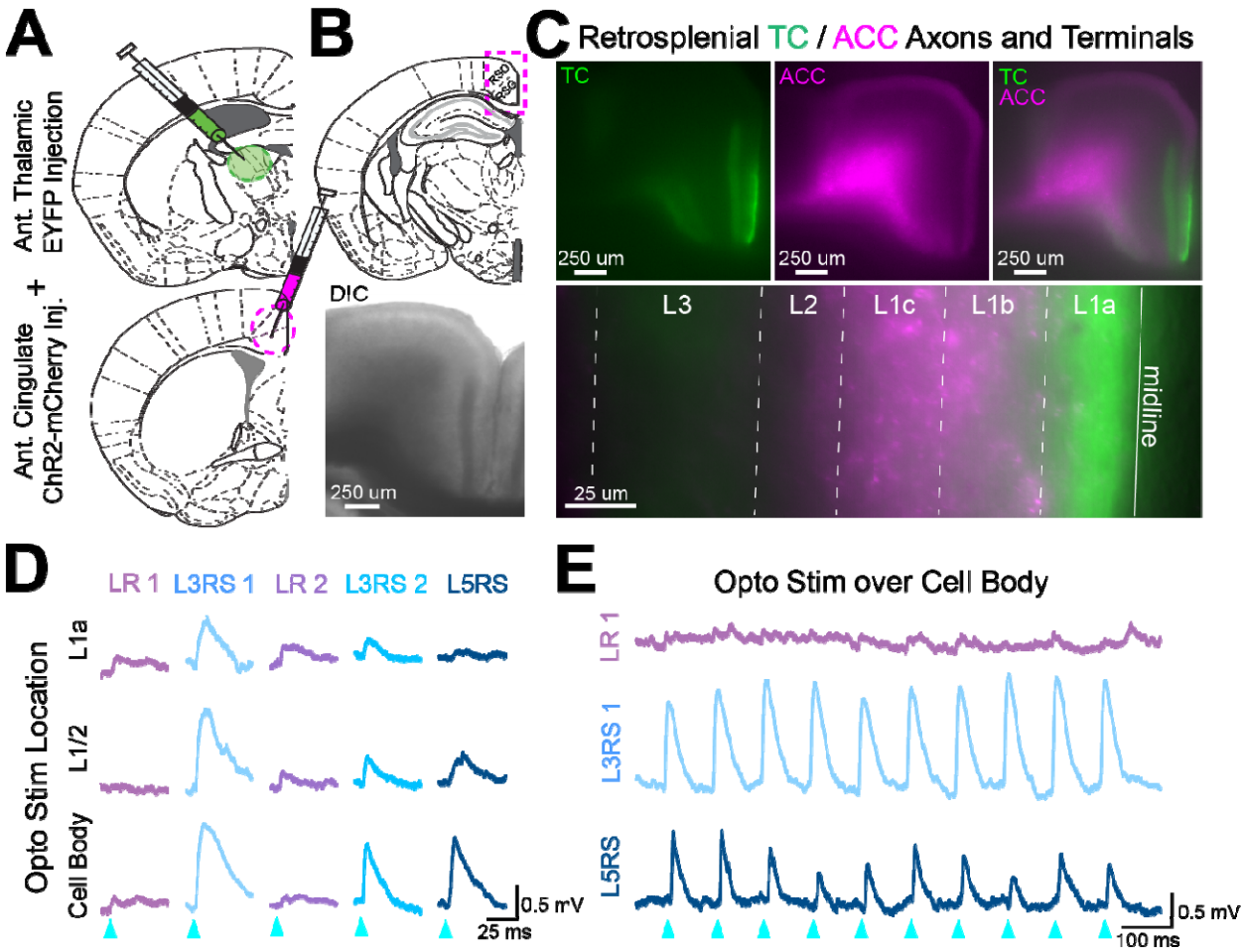

Figure S5. Layer 3 and 5 RS neurons in RSG exhibit larger postsynaptic responses to corticocortical inputs from the anterior cingulate cortex (ACC) than LR neurons. (Related to Figures 5&6)

- ***A.*** Schematic showing the dual injection of the optogenetic viral construct into anterior cingulate cortex (ACC) and a fluorescent eYFP tag into AD/AV (see Methods).
- ***B.*** Top: Schematic of the target recording region, RSG. Bottom: DIC image of the RSG brain slice.
- ***C.*** Top left: Epiflorescent image of the AD/AV axonal and terminal arborizations in RSG. Top middle: Epiflorescent image of the ACC axonal and terminal arborizations in RSG. Top right: Overlay of AD/AV (green) and ACC (magenta) axonal and terminal arborizations in RSG. Bottom: 60x image of the superficial layers of RSG, showing the brightest expression of magenta ACC axons in layers 1b, 1c, and 3, and brightest expression of green AD/AV axons in layers 1a and dimly in 3. Layers are demarcated by dotted white lines.
- ***D.*** Example EPSP traces of 5 same-slice sequentially patched neurons (LR: purple, n = 2; L3RS, blue, n = 2; L5RS: navy, n = 1) when responding to optogenetic activation of the CC arbors at the cell body, L1/2, and L1a in standard ACSF. Blue arrow marks LED-based optogenetic pulse. L3 and L5 RS neuron responses are larger than LR responses at both L1/2 and cell body stim locations, and L3 RS cell responses are also larger than LR responses at L1a stim. Cells were held at -65 mV.
- ***E.*** Trace examples from LR1 (purple), L3 RS1 (blue), and L5 RS (navy) from ***D*** showing responses to 10 Hz train of 1 ms wide optogenetic LED pulses. Blue triangles indicate each LED pulse. Cells were held at -65 mV.

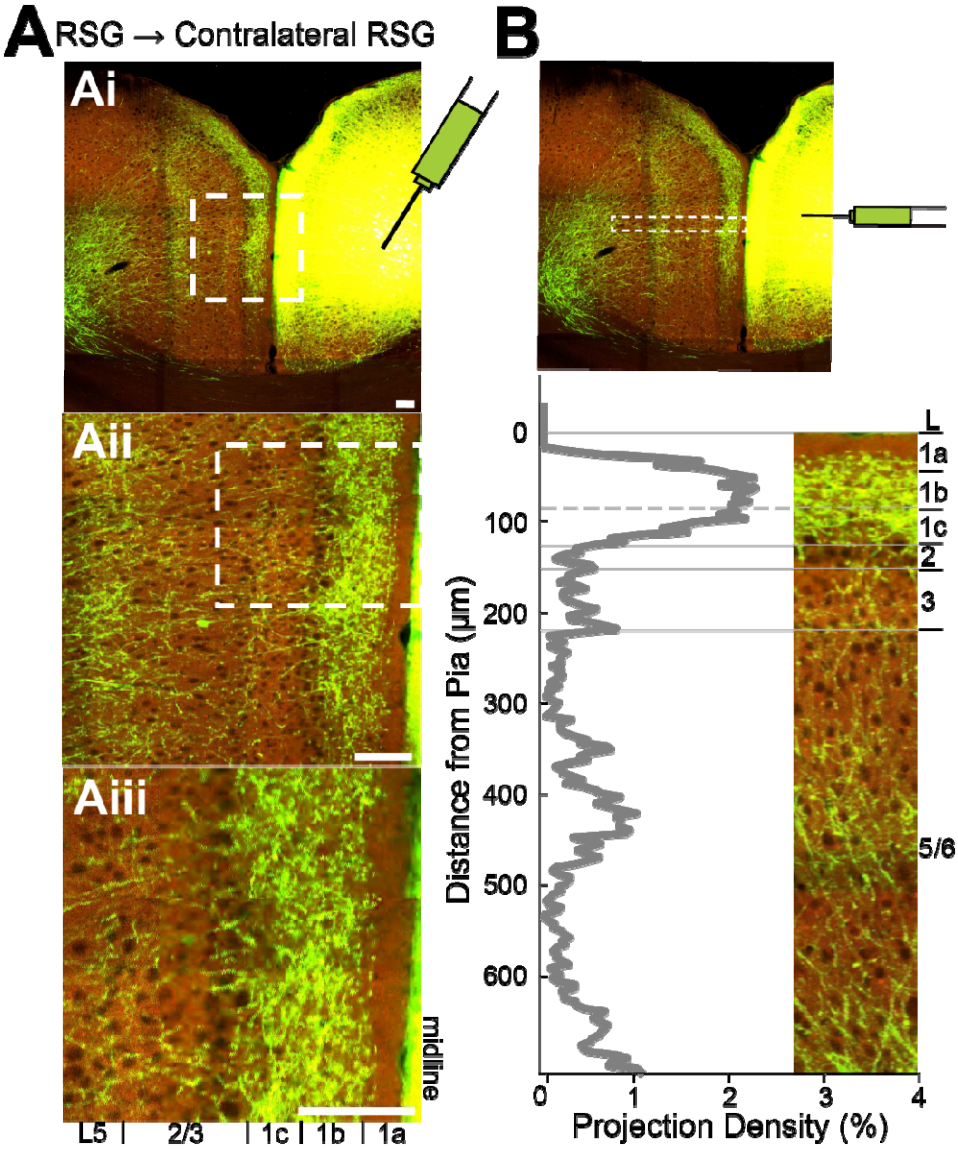

Figure S6. Contralateral RSG projections preferentially terminate in deep, but not superficial, parts of RSG layer 1. (Related to Discussion) The image of axonal projection patterns was obtained from the Allen Mouse Brain Connectivity Atlas (https://connectivity.brain-map.org; Oh et al., 2014). RSG (experiment #100140949), image #81, as numbered in high resolution image viewer, was used.

Ai. Anterograde injection into right hemisphere of RSG labels contralateral projections.

Aii. Contralateral projections follow a defined lamination pattern with strong band of expression in layer 1.

Aiii. Within RSG L1, contralateral projections preferentially terminate in deep L1b/c, while avoiding superficial L1a. Abbreviations: RSG – granular retrosplenial cortex, L – layer. Scalebar: 70 µm

B. Top: Schematic of injection into right hemisphere of RSG. Box defines the location of image in lower panel. Bottom: Projection density plot of contralateral RSG axons and terminal arbors.

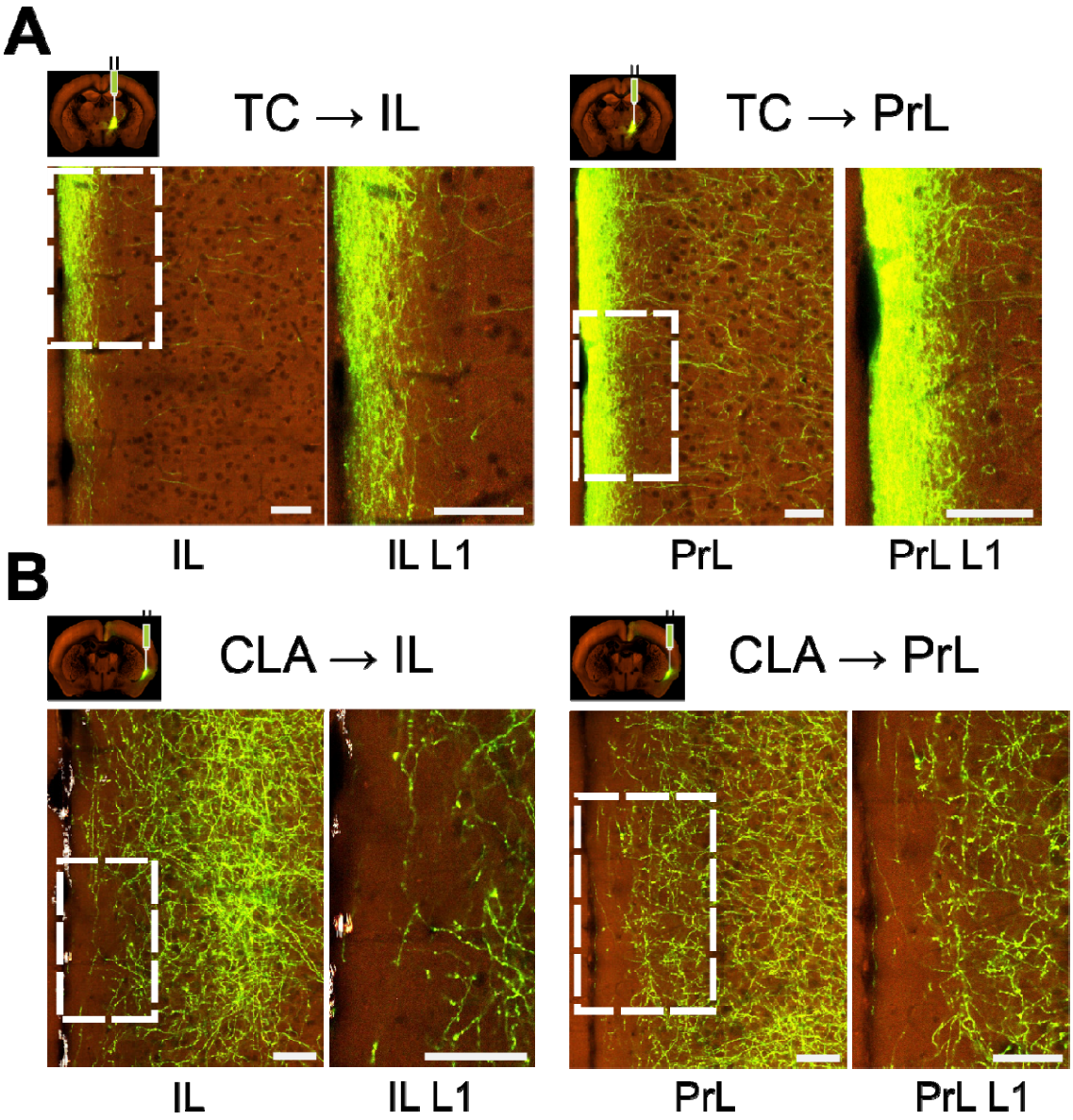

Figure S7. Sublaminar differences in thalamic vs claustral projections to medial prefrontal cortex. (Related to Discussion) Each panel shows overview of expression in a cortical area (left) and its layer 1 only (right). Images of axonal projections patterns were obtained from the Allen Mouse Brain Connectivity Atlas (https://connectivity.brain-map.org; Oh et al., 2014). The following images, as numbered in high resolution image viewer, were used: for TC, ventromedial nucleus (VM; experiment #127797441), image #69 for injection and #36 for PrL and IL; for CLA (experiment #485903475) image #56 for injection and #31 for PrL and IL. Abbreviations: TC - thalamocortical, CLA - claustrum, PrL - prelimbic cortex, IL - infralimbic cortex, L1 - layer 1. Scale bar: 70 µm

- ***A.*** Axonal projection expression in infralimbic and prelimbic cortices from anterograde injection into ventromedial thalamus. Projections show strong preference for superficial parts of layer 1.
- ***B.*** Axonal projection expression in infralimbic and prelimbic cortices from anterograde injection into claustrum. Higher density of projections can be observed at deep layer 1, while very few axons reach superficial-most parts.

Table S1. P-Values for intrinsic property comparisons across cell types.	LR v. L3 RS p-values	LR v. L5 RS p-values	L3 RS v. L5 RS p-values
Postnatal age at time of recording (days)	0.6251	0.0767	0.2249
Resting membrane potential (mV)	0.0122 *	0.0311 *	0.9245
Input resistance (MΩ)	5.66e-12 ***	4.47e-13 ***	0.234
Input capacitance (pF)	1.20e-13 ***	1.81e-14 ***	0.0412 *
Membrane time constant (ms)	0.1096	0.0639	0.6916
Action potential threshold (mV)	0.3137	0.1170	0.7826
Action potential amplitude (mV)	0.0000138 ***	3.12e-07 ***	0.2887
Action potential width (ms)	2.36e-07 ***	6.40e-08 ***	0.6947
Spike frequency adaptation ratio	9.40e-11 ***	3.60e-10 ***	0.9058
Latency to first spike (ms)	0.3271	0.0000539 ***	0.0341 *
Rheobase (pA)	0.000119 ***	3.86e-09 ***	0.0673

Table S1. P-values for intrinsic property comparisons across cell type. (Related to Table 1) All p-values for statistical significance between cell types for the intrinsic properties calculated and reported in Table 1. Wilcoxon rank sum test was used for all comparisons.

	ADAV arbors	CLA arbors	LR cell 1	LR cell 2	LR cell 3	LR cell 4	LR cell 5	LR cell 6	RS cell 1	RS cell 2	RS cell 3	RS cell 4	RS cell 5
ADAV arbor	0	4.04E-05	2.50E-21	8.69E-13	1.04E-05	3.15E-14	1.18E-20	5.00E-18	7.38E-03	6.72E-01	4.30E-02	1.07E-02	3.56E-01
CLA arbor	4.04E-05	0	1.09E-01	5.95E-02	1.18E-01	4.76E-02	4.74E-02	6.06E-02	1.13E-05	1.50E-02	1.39E-02	2.27E-02	5.46E-03
LR cell 1	2.50E-21	1.09E-01	0	1.33E-32	2.02E-31	1.84E-12	3.20E-57	5.25E-32	1.55E-01	7.20E-01	2.27E-01	2.01E-01	3.46E-01
LR cell 2	8.69E-13	5.95E-02	1.33E-32	0	4.96E-19	2.55E-07	5.10E-44	6.91E-14	3.98E-01	2.91E-01	6.33E-01	5.93E-01	8.43E-01
LR cell 3	1.04E-05	1.18E-01	2.02E-31	4.96E-19	0	1.35E-10	1.12E-44	6.02E-40	1.75E-01	5.39E-01	2.25E-01	1.68E-01	1.79E-01
LR cell 4	3.15E-14	4.76E-02	1.84E-12	2.55E-07	1.35E-10	0	1.12E-19	2.11E-20	2.36E-01	9.00E-01	2.95E-01	1.79E-01	5.57E-01
LR cell 5	1.18E-20	4.74E-02	3.20E-57	5.10E-44	1.12E-44	1.12E-19	0	2.27E-38	8.17E-02	9.12E-01	1.89E-01	1.29E-01	4.39E-01
LR cell 6	5.00E-18	6.06E-02	5.25E-32	6.91E-14	6.02E-40	2.11E-20	2.27E-38	0	1.33E-01	4.11E-01	1.26E-01	9.94E-02	1.88E-01
RS cell 1	7.38E-03	1.13E-05	1.55E-01	3.98E-01	1.75E-01	2.36E-01	8.17E-02	1.33E-01	0	2.21E-48	6.00E-75	4.99E-49	7.03E-46
RS cell 2	6.72E-01	1.50E-02	7.20E-01	2.91E-01	5.39E-01	9.00E-01	9.12E-01	4.11E-01	2.21E-48	0	8.94E-52	3.79E-28	8.38E-42
RS cell 3	4.30E-02	1.39E-02	2.27E-01	6.33E-01	2.25E-01	2.95E-01	1.89E-01	1.26E-01	6.00E-75	8.94E-52	0	3.78E-46	1.26E-52
RS cell 4	1.07E-02	2.27E-02	2.01E-01	5.93E-01	1.68E-01	1.79E-01	1.29E-01	9.94E-02	4.99E-49	3.79E-28	3.78E-46	0	7.55E-53
RS cell 5	3.56E-01	5.46E-03	3.46E-01	8.43E-01	1.79E-01	5.57E-01	4.39E-01	1.88E-01	7.03E-46	8.38E-42	1.26E-52	7.55E-53	0

Table S2. P-values for dendritic and afferent arbor correlation analyses. (Related to Figures 2&5 and Figure S2) All p-values for statistical significance between: (1) apical dendritic lamination correlations between and within cell types, and (2) correlations between apical dendritic and afferent arbor lamination.